Doctor of Philosophy

ELECTRICALLY ASSISTED PRESSURE JOINING OF

SIMILAR AND DISSIMILAR METAL ALLOYS

The Graduate School of the University of Ulsan

School of Mechanical Engineering

Yong-Fang Li

ELECTRICALLY ASSISTED PRESSURE JOINING OF

SIMILAR AND DISSIMILAR METAL ALLOYS

Advisor: **Sung-Tae Hong**

A Dissertation

Submitted to the Graduate School of the University of Ulsan
in Partial Fulfillment of the Requirements
for the Degree of

Doctor of Philosophy

by

Yong-Fang Li

School of Mechanical Engineering
University of Ulsan, South Korea
December 2019

Yong-Fang Li 의

공학박사 학위 논문을 인준함

심사위원	천두만	(인)
심사위원	홍성태	(인)
심사위원	김문조	(인)
심사위원	정구현	(인)
심사위원	김동규	(인)

울 산 대 학 교 대 학 원
기계자동차공학과
2019 년 12 월

ELECTRICALLY ASSISTED PRESSURE JOINING OF

SIMILAR AND DISSIMILAR METAL ALLOYS

The certifies that the dissertation of

Yong-Fang Li is approved

Committee Chair   Professor Doo-Man Chun

Committee member   Professor Sung-Tae Hong

Committee member   Dr. Moon-Jo Kim

Committee member   Professor Koo-Hyun Chung

Committee member   Professor Dong-Kyu Kim

School of Mechanical Engineering

University of Ulsan, South Korea

December 2019

ABSTRACT

Metals are the most widely used materials for fabrication of products. Metal joining, as one of the key manufacturing technologies, is used extensively in production and plays predominant roles in manufacturing industry. Electrically assisted pressure joining (EAPJ) is one of the electrically assisted manufacturing (EAM) techniques. EAM is a new concept for manufacturing processes that utilize the electroplasticity of metals and their alloys to improve productivity, efficiency, and quality. EAPJ using resistance heating as a heat source is a solid state joining without melting or solidification. In this dissertation, the feasibility and effectiveness of EAPJ on similar and dissimilar metal materials are investigated.

Firstly, EAPJ of a Grade 1 titanium (Ti) alloy sheet with thickness of 1 mm is experimentally investigated. In this study, a custom-made EAPJ apparatus is developed for testing different process conditions. During joining process, an electric current is directly applied to the lap joint specimens during plastic compressive deformation. The optical microscopy (OM) and electron back-scatter diffraction (EBSD) results confirm that defect-free joints are successfully fabricated in the selected Ti alloy. The shear tensile test results show that the joint strength and fracture modes are strongly affected by the EAPJ process conditions, such as the amount of plastic deformation and the electric current intensity. The result of present study shows that the EAPJ is efficiently applicable to joining of Ti alloy sheets.

Next, a study on the EAPJ of bulk workpieces, stainless steel 316L (SUS316L) cylindrical specimens, is carried out. An additive manufactured (AM) metal porous interlayer is used in the study to improve the process effectiveness for the EAPJ of

cylindrical bulk components. The AM porous interlayer is fabricated using SUS316L powder by metal additive manufacturing (or simply, 3D printing) with selective laser melting. During EAPJ, axial compression and an electric current were simultaneously applied to the specimen assembly. The OM and EBSD results show that any of the EAPJ joints with or without the porous interlayer is successfully fabricated. A lower joining pressure is needed when applying the AM metal porous interlayer with a lower compressive strength and higher electric resistivity. In the present study, the practicability and effectiveness for the EAPJ of cylindrical bulk components are demonstrated by using an AM metal porous interlayer.

Finally, EAPJ of dissimilar materials, SUS316L and Inconel 718 (IN718) cylindrical bulk specimens, is experimentally investigated. The specimen assembly for the experiment comprises two cylindrical solid specimens (SUS316L and IN718), with an identical geometry. In EAPJ, electric current and plastic compression are directly applied to the specimen assembly simultaneously. The microstructural analysis (FE-SEM with EBSD and EDS) confirms that defect-free joints are successfully fabricated by EAPJ in the selected dissimilar metal alloys without melting and solidification. Obvious atomic diffusion region at the interface of the EAPJ joint is identified. The results of tensile tests show that all the joints fracture from SUS316L alloy side, which undergoes typical ductile fracture with severe plastic deformation prior to fracture. The result of the present study confirms that the concept of EAPJ is efficiently applicable to solid state joining of dissimilar material combination.

ACKNOWLEDGMENTS

TABLE OF CONTENTS

LIST OF FIGURES

ix

LIST OF TABLES

CHAPTER Ⅰ

INTRODUCTION

Joining technology plays a prominent role in modern manufacturing technologies since it is hardly conceivable to manufacture a product without some sort of joining due to functional needs and technological limitations (Martinsen *et al.*, 2015). As the scale and complexity of products such as aircraft, automobile and train increase, demand for joining of similar and dissimilar materials grows. Also, some new and superior joining methods are needed to satisfy more commercial requirements of higher performance, higher productivity and lower cost in joining operations (Mori *et al.*, 2013). Generally, joining processes can be classified into three categories: metallurgical joining, adhesive bonding and mechanical fastening (Mori *et al.*, 2013).

Adhesive bonding is usually used to join two parts together by using glues, epoxies, or various plastic agents. In this joining technology, little or no heat is needed to create the joint. As a result, the material structure of the joints is not macroscopically affected, deformations or internal stress is also rarely occurred (Brockmann *et al.*, 2009). However, one major disadvantage of adhesive bonding is the relatively poor heat resistance of the bond line as compared to inorganic materials such as metal or glass (Brockmann *et al.*, 2009). The strength of the adhesive bonded joints is almost always lower than that achieved by metallurgical joining (Mori *et al.*, 2013).

Mechanical fastening is a widely used method to join various materials, such as metal, plastics and composites. This joining technology contains a range of processes that utilize a

variety of fasteners including nuts and bolts, screws and rivets, or mechanical interlocks to assemble materials without heating (Speck, 2015). In contrast to the metallurgical joining processes, the chemical composition and microstructure are unchanged since no atomic or molecular level bonding is created between the components being joined (Jr RWM, 1993). Mechanical fastening exists some disadvantages, such as stress concentrations at holes, possible of galvanic corrosion, loosening, additional weight, high cost and so on. Mechanical fastening is often preferred for joining of dissimilar materials and polymer-matrix composites that are sensitive to extreme heat.

Metallurgical joining is commonly used to join metals in the fabrication of structures. In this joining process, mechanical bonding takes place at the original boundary surfaces of two pieces of metal to be joined (Campbell, 2011). Basically, this technology is used for making permanent joints by heating them to a suitable temperature with or without the application of pressure. Metallurgical joining is used in the manufacture of automobile bodies, aircraft frames, railway wagons, machine frames, structural works, tanks, furniture, boilers, general repair work and ship building (Akca *et al.,* 2016). Usually, metallurgical joining processes can be divided into two major categories: fusion joining and solid-state joining.

In fusion joining processes (e.g., tungsten inert gas welding, electron beam welding and electric resistance spot welding), the metal parts are melted and joined together forming a joint after solidification. Distortion and residual stress are generally generated due to the existence of melting and solidification during this joining (Campbell, 2011). The microstructure and properties of the joint area are different from the parent metal. Usually, three predominant zones are involved in fusion joining: the nugget zone, a heat-affected

zone (HAZ), and the base metal (Campbell, 2011). The nugget forms the as-cast structure with a complex composition. The HAZ is always considered as the weak portion in the joint due to grain growth induced by the high temperature. Bonding dissimilar metals by fusion joining is challenging task, especially when the metals have substantially different melting point and coefficient of thermal expansion, such as steel and aluminum alloys.

In contrast to fusion joining, solid-state joining does not involve the melting of materials. In this process, two workpieces are joined under a pressure providing an intimate contact between them and at a temperature essentially below the melting point of the parent material. Because of no melting and solidification, solid-state joining provides comparatively lower lever of distortion and residual stress generation. The parent metals essentially retain their original properties and the HAZ problems are significantly diminished. Also the formation of intermetallic phases at the interface which can be brittle and may yield corrosion concerns is largely eliminated or minimized (Akca *et al.,* 2016). Furthermore, during joining of dissimilar metals, their thermal expansion and conductivity characteristics have much less influence on the resulting joint performance than with fusion welding processes (Akca *et al.,* 2016). Therefore, except similar metals, solid-state joining is useful to join dissimilar metal couples, in particular, with a large difference in physical and mechanical properties, such as steel-aluminum, steel-copper, aluminum-titanium and other materials that are difficult to join by fusion joining (Kumai *et al.,* 2014).

Solid-state joining includes friction stir welding, pressure joining, forge joining, roll joining, friction joining, diffusion joining, explosion joining and so on. Except for friction stir welding, which generates a solid-state joint resulting from the mechanical stirring of metals using a rotating tool, other solid-state joining processes generally use the same

3

bonding mechanism of pressure joining, which generates joints by establishing diffusion bonding between metal surfaces under pressure.

The most widely accepted mechanism for pressure joining is the film theory (Mohamed *et al.,* 1975; Bay *et al.,* 1979). Metal surfaces are covered with oxide layers, which prohibit metallic bonding between two contacting surfaces. During pressure joining, metals are compressed against each other and deformed. As a result, the oxide layers break and many micro-cracks on the metals surface are formed. The virgin metals are then extruded through these micro-cracks and contact with each other until a metallic bond is established at the interface. Therefore, pressure joining establishes metallurgical bonds between two clean and intimately contacting metallic surfaces under pressure without the formation of a liquid phase (Sahin *et al.,* 2012).

Pressure (plastic deformation), temperature and time are the most important process parameters in pressure joining. Mahabunphachai *et al.* (2009) found that the bond strength significantly depends on the amount of plastic deformation in pressure joining. Threshold deformation is existed to initiate a bond of two metal parts. As the deformation increases, the bond strength will progressively increase to a maximum point at an optimal deformation value followed by a decrease, due to excessive reduced cross section of the two bonded parts (Mahabunphachai *et al.,* 2009). Also, temperature is a key factor in pressure joining. Some metal alloys, such as aluminum and copper alloys, can be joined successfully at ambient temperature under a pressure with a substantial deformation (Ozel *et al.,* 2008). However, some metals can only be jointed at elevated temperature, such as magnesium alloys, stainless steel, and nickel alloys. Magnesium alloys normally exhibit low ductility near room temperature because of their h.c.p structure. Somekawa *et al.* (2003) investigated the

superplastic characteristic and diffusion bonding behavior of commercial magnesium AZ31 alloys at temperatures between 623 K to 723 K. Mahabunphachai *et al.* (2009) successfully bonded the thin sheets of nickel to nickel and stainless steel to stainless steel with the initial thickness of 51 μm at elevated temperature levels of 150 ℃ and 300 ℃, which could not be joined in the cold condition.

In conventional pressure joining, complex heating and control facilities such as induction heating furnace and electrical resistance heating furnace are always required for achieving a more controlled temperature. However, such heating method inevitably heats up the regions which do not need heating. Also, the acceptable size of any workpieces involved in this joining process is limited to the size of the furnace. To overcome such drawbacks, electrically assisted pressure joining (EAPJ) using resistance heating as a heat source is suggested (Peng *et al.,* 2013). EAPJ is one of the electrically assisted manufacturing (EAM) technologies.

EAM is a new metal manufacturing technique which can enhance formability of metal alloys during deformation and reduce springback after deformation (Salandro *et al.,* 2015). In this method, electric current is directly applied to a metal specimen during deformation. The effect induced by electric current during deformation has been defined as electroplasticity, which has been attributed to some hypotheses. Firstly, localized atomic-level resistive heating effects are enhanced by the resistivity of the material, for example, electrons scatter off of interfacial defects within the lattice, such as voids, impurities, grain boundaries (Roth *et al.,* 2008). This heating occurs on the atomic level (within the metal's lattice), and although this contributes toward the overall heating of the workpiece, this temperature increase is not the same as the bulk temperature increase that is witnessed at the

5

part's surface (known as global or bulk heating) (Salandro *et al.,* 2015). Specifically, the bulk temperature of a metal is the result of all the atomic-level heating locations. This effect expands the local lattice and allows for easier dislocation motion (i.e., plastic deformation) by way of enhanced diffusion (Salandro *et al.,* 2015). Secondly, direct dislocation–electron interaction takes place as the flowing electrons impact the dislocation lines, assisting in "pushing" the dislocation lines and further enhancing plastic deformation and material ductility (Yao *et al.,* 1996). This can be used to explain why the temperature of an EA forming test, where electricity is applied during deformation, is less than a stationary electrical test, where the electricity is applied when no deformation takes place. In the EA forming, some of the energy is used to assist plastic deformation, instead of fully contributing toward resistive heating (Salandro *et al.,* 2015). Finally, the addition of excess electrons to the microstructure of metal is an important aspect. Since the electron clouds control how strongly a metal is bonded and essentially act as the "glue" which holds a metal together, the excess electrons (obtained from applying the electricity) will assist in breaking and reforming bonds by reducing the bond strength between electrons (Salandro *et al.,* 2015). As the metallic bonds are able to break and reform easier, the ductility of the metal is improved; hence, it becomes more workable (Antolovich *et al.,* 2004).

Although the exact mechanism of the electroplastic effect is still under debate (Hariharan *et al.,* 2017), experiments confirm that the electroplastic effect cannot solely be attributed to the associated Joule heating and the interaction between moving electrons and dislocations also play a role (Conrad, 2000; Kopanev, 1991). The suggested EAM processes (Nguyen-Tran *et al.,* 2015) are mainly associated with bulk deformation (e.g., EA forging (Jones *et al.,* 2012), EA rolling (Xu *et al.,* 2007) and EA drawing (Stashenko *et al.,* 2009)),

sheet-metal forming (e.g., EA deep drawing (Wang, 2009), EA embossing (Mai *et al.,* 2013) and EA blanking (Kim *et al.,* 2014)), EA joining (e.g. EA friction stir welding (Potluri *et al.,* 2013) and EAPJ (Peng *et al.,* 2013)) and EA cutting (Baranov *et al.,* 2011).

EAPJ is a solid-state joining without melting in contrast to the resistance spot welding, which is one of fusion joining technologies with melting and solidification. In comparison to conventional pressure joining, EAPJ has several technical advantages. The workpieces can be heated rapidly and locally. As a result, the process time can be reduced and unnecessary thermal effects on the workpiece can be minimized. Also, the joining apparatus can be significantly simpler and cost-effective due to the need for a heating furnace is eliminated.

However, little research has been done in EAPJ so far. The studies on EAPJ of metal alloys are mostly focused on very thin foils. Ng *et al.* (2015) applied electrically assisted roll bonding process to bond 127 μm aluminum sheet to 127 μm aluminum or 127 μm copper sheets. Xu *et al.* (2014) successfully joined SUS316L foils with thickness of 100 μm using EAPJ. Peng *et al.* (2013) conducted EAPJ of brass to brass (CuZn40) and SUS316L to SUS316L with different thicknesses of 100 μm and 150 μm. In practice, except thin foil specimens, EAPJ can be also used to join structural plates and bulk workpieces. Especially, in the joining of bulk components, EAPJ also provides technical advantages over friction joining that is usually considered for joining cylindrical parts. For example, friction joining requires a relatively expensive and complex brake system since the rotation of a workpiece must be stopped completely and rapidly for successful joining (Kimura *et al.,* 2017). Also, there is no additional frictional heat generated during the actual generation of a solid-state joint since the rotation ceases prior to the final axial compression during friction welding. However, in EAPJ using resistance heating as a heat source, the need for complex rotation

and brake systems can be eliminated. Also, since the heating of the interface can be continued during the final axial compression, process optimization is relatively easier. In the present study, EAPJ of structural sheets of 1 mm thick Grade 1 Ti alloy (chapter Ⅱ), EAPJ of bulk components of cylindrical SUS316L with and without metal porous interlayer (chapter Ⅲ), and EAPJ of dissimilar materials (SUS316L and IN718) with and without metal porous interlayer (chapter Ⅳ) are experimentally investigated. Chapter Ⅱ to Ⅳ are presented as three independent journal papers which have been published.

In chapter Ⅱ, EAPJ of Ti alloy sheets is experimentally investigated. In this study, Grade 1 titanium (Ti) alloy sheets with thickness of 1 mm were lap joined by EAPJ. The cross-sectional microstructure of EAPJ joints was characterized by OM and EBSD. The joint strength and fracture modes are examined under lap shear tensile tests. The suitability of EAPJ for the selected Ti alloy was evaluated along with the effects of joining parameters on the joint performance to provide guidance for process optimization.

In chapter Ⅲ, EAPJ of bulk components of cylindrical SUS316L is experimentally investigated. In order to further concentrate the resistance heat on the joint interface and reduce the required joining pressure, the effectiveness of EAPJ of cylindrical SUS316L using an additive manufactured (AM) porous interlayer between the two solid specimens was also investigated. The metal porous interlayer was fabricated using SUS316L powder by metal additive manufacturing (or simply, metal 3D printing) with selective laser melting. During the joining process, an electric current is directly applied to the specimen assembly while the specimen assembly is under continuous axial compression. The cross sectional microstructure along the joining direction was analyzed by OM and EBSD. To confirm a sufficient joint strength, the joints were machined to cylinders with a diameter of 8 mm and

simple cantilever bend tests were conducted. The result of the present study can be expanded to solid-state joining of dissimilar (or even difficult to weld) bulk components by properly adjusting the structure and chemical composition of the porous interlayer (Hong *et al.,* 2017).

In chapter Ⅳ, EAPJ of dissimilar bulk workpieces is experimentally investigated. In this study, dissimilar metals of SUS316L and IN718 cylindrical specimens with an identical geometry were prepared for EAPJ. For EAPJ, the resistance heating was induced by a non-continuous electric current during compression. The cross section of the dissimilar joint was prepared along the joining direction for microstructural analysis (FE-SEM with EBSD and EDS). The mechanical properties of the dissimilar joint were evaluated by Vickers hardness measurements on the cross section along the center line in the joining direction using a Vickers indenter. To further confirm sufficient joint strength, uniaxial tensile tests were carried out. The result of the present study confirms that the concept of EAPJ is applicable to solid state joining of dissimilar material combination.

References

Akca E, Gursel A (2016) Solid state welding and application in aeronautical industry. Periodicals of Engineering and Natural Sciences 4(1):1-8.

Antolovich SD, Conrad H (2004) The effects of electric currents and fields on deformation in metals, ceramics, and ionic materials: an interpretive survey. Materials and Manufacturing Processes 19(4):587–610.

Baranov SA, Staschenko VI, Sukhov AV, Troitskiy OA, Tyapkin AV (2011) Electroplastic metal cutting. Russian Electrical Engineering 82(9):477-479.

Bay N (1979) Cold pressure welding-the mechanisms governing bonding. Journal of Engineering for Industry 101(2):121–127.

Brockmann W, Geiß, PL, Klingen J, Schröder B (2009) Adhesive bonding: materials applications and technology. WILEY-VCH Verlag GmbH & Co. KGaA, Weinheim.

Campbell FC (2011) Joining: Understanding the basics. ASM International, Ohio.

Conrad H (2000) Electroplasticity in metals and ceramics. Materials Science and Engineering A 287(2):276-287.

Hariharan K, Kim MJ, Hong ST, Kim D, Song JH, Lee MG, Han HN (2017) Electroplastic behaviour in an aluminium alloy and dislocation density based modelling. Materials & Design 124(15):131:142.

Hong ST, Chun DM, Park HS, Han HN, Park JW, Li YF, Nguyen DS (2017) Electrically Assisted Pressure Joining Apparatus and Method. KR Patent pending No. 10-2017-0079198.

Jones, JJ, Mears L, Roth JT (2012) Electrically-assisted forming of magnesium AZ31: effect of current magnitude and deformation rate on forgeability. Journal of Manufacturing Science and Engineering 134(3):034504,1-7.

Jr RWM (1993) Joining of advanced materials. Butterworh-heinemann, a division of Reed publishing Inc, New York.

Kim W, Yeom KH, Thien NT, Hong ST, Min BK, Oh S, Kim MJ, Han HN, Lee HW (2014) Electrically assisted blanking using the electroplasticity of ultra-high strengh metal alloys. CIRP Annals-Manufacturing Technology 63(1):273-276.

Kimura M, Suzuki K, Kusaka M, Kaizu K (2017) Effect of friction welding condition on joining phenomena and mechanical properties of friction welded joint between 6063 aluminium alloy and AISI 304 stainless steel. Journal of Manufacturing Processes 26:178-187.

Kopanev AA (1991) The nature of the electroplastic effect in metals. Strength of Materials 23(1):55-59.

Kumai S (2014) Dissimiar-matal joining using several types of high-speed solid-state welding methods. Mertials Science Forum 794-796:357-364.

Mahabunphachai S, Koc M, Ni J (2009) Pressure Welding of Thin Sheet Metals: Experimental Investigations and Analytical Modeling. Journal of Manufacturing Science and Engineering, 131(4):041003, 1-9.

Mai J, Peng L, Lai X, Lin Z (2013) Electrical-assisted embossing process for fabrication of micro-channels on 316L stainless steel plate. Journal of Maerials Processing Technology 213(2):314-321.

Martinsen K, Hu SJ, Carlson BE (2015) Joining of dissimilar materials. CIRP Annals-Manufacturing Technology 64(2):679-699.

Mohamed HA, Washburn J (1975) Mechanism of solid state pressure welding. Weld Journal 302–310.

Mori K, Bay N, Fratini L, Micari F, Tekkaya AE (2013) Joining by plastic deforming. CIRP Annals-Manufacturing Technology 62(2):673-694.

Ng MK, Li L, Fan Z, Gao RX, Smith III EF, Ehmann KF, Cao J (2015) Joining sheet metals by electrically-assisted roll bonding. CIRP Annals-Manufacturing Technology 64(1):273–276.

Nguyen-Tran HD, Oh HS, Hong ST, Han HN, Cao J, Ahn SH, Chun DM (2015) A review of electrically-assisted manufacturing. International Journal of Precision Engineering and Manufacturing-Green Technology 2(4):365-376.

Ozel K, Sahin M, Akdogan A (2008) Mechanical and metallurgical properties of aluminium and copper sheets joined by cold pressure welding. Journal of Mechanical Engineering 54(11):796-806.

Peng L, Xu Z and Lai X (2013) An investigation of electrical-assisted solid-state welding/bonding process for thin metallic sheets: Experiments and modeling. Proceedings of the Institution of Mechanical Engineers Part B Journal of Engineering Manufacture 228(4): 582-594.

Potluri H, Jones JJ, Mears L (2013) Comparison of electrically-assisted and conventional friction stir welding processes by feed force and torque. Proc. Of ASME International Manufacturing Science and Engineering Confernece Collocated with

the 41th North American Manufacturing Research Conference, Paper No. MSEC2013-1192.

Roth JT, Loker I, Mauck D, Warner M, Golovashchenko SF, Krause A (2008) Enhanced formability of 5754 aluminum sheet metal using electric pulsing. Transactions of the North American Manufacturing Research Institution of SME 36:405–412

Sahin M, Misirli C (2012) Properties of cold pressure welded aluminium and copper sheets. Advanced Materials Research 463-464:244-248.

Salandro WA, Jones JJ, Bunget C, Mears L, Roth JT (2015) Electrically assisted forming: modeling and control. Springer International Publishing, Swizerland.

Somekawa H, Hosokawa H, Watanabe H, Higashi K (2003) Diffusion bonding in superplastic magnesium alloys. Materials Science and Engineering: A 339(1-2): 328-333.

Speck JA (2015) Mechanical fasenting, Joining, and assembly, 2nd ed. Taylor & Francis Group, LLC CRC Press, Florida.

Stashenko V, Troitskii O, Novikova N (2009) Electroplastic drawing medium-carbon steel. Journal of Machinery Manufacture and Reliability 38(4):369-372.

Wang S (2009) Effect of electric pulses on drawability and corrosion property of AZ31 magnesium alloy. M.Sc. Thesis, Materials Science and Engineering, Tsinghua University.

Xu Z, Peng L, Lai X (2014) Electrically assisted solid-state pressure welding process of SS 316 sheet metals. Journal of Materials Processing Technology 214(11):2212–2219.

Xu Z, Tang G, Tian S, Ding F, Tian H (2007) Research of electroplastic rolling of AZ31 Mg alloy strip. Journal of Materials Processing Technology 182(1):128-133.

Yao L, Hong C, Yunquo G, Xinbin H (1996) Effect of electric current pulse on superplasticity of aluminum alloy 7475. Transactions of Nonferrous Metals Society of China. 6(1):77–84.

CHAPTER Ⅱ

ELECTRICALLY ASSISTED PRESSURE JOINING OF TITANIUM ALLOYS

ABSTRACT

Electrically assisted pressure joining (EAPJ) of a Grade 1 titanium (Ti) alloy is experimentally investigated. In EAPJ, an electric current is directly applied to the specimen during plastic compression. Microstructural analysis shows that solid-state joints are successfully fabricated in the selected Ti alloy without melting. Shear tensile tests shows that the strength and fracture modes of the joint are strongly affected by a combination of the amount of plastic deformation (corresponding to a thickness reduction) and the electric current intensity. An optimal thickness reduction, corresponding to the maximum fracture load, exists for each value of current intensity, and decreases as current intensity increases. A higher fracture load can be obtained by adjusting the combination of the current intensity and the thickness reduction parameters.

Keywords: Electrically assisted pressure joining; Titanium alloy; Joint strength; Solid-state joint

2.1 Introduction

Due to their excellent properties such as moderately high specific strength, high fatigue life, high toughness, good formability, and excellent corrosion resistance, titanium (Ti) alloys are used in a wide range of industries, including aerospace, automotive, and biomedical (Baydaba *et al.,* 2016; Mohammed *et al.,* 2017). However, to further expand the applications of Ti alloys, proper joining is an important issue. Joining processes can be divided into two major categories: fusion joining (e.g., arc welding (Lathabai *et al.,* 2001) and electron beam welding (Saresh *et al.,* 2007)) and solid-state joining (e.g., friction stir welding (Fujii *et al.,* 2010; Lee *et al.,* 2005) and pressure welding (Mohamed *et al.,* 1975; Bay *et al.,* 1979)). In general, fusion joining of Ti alloys can be challenging since Ti alloys become highly reactive in the molten state, and their mechanical properties decline due to the formation of Ti oxide and porosity in the weld bead.

Solid-state joining is an alternative to fusion joining for Ti alloys. For example, pressure joining (Mohamed *et al.,* 1975; Bay *et al.,* 1979) can result in good joint performance with low cost, high accuracy, high efficiency, and minimal damage to the surrounding parts of the material. The most widely accepted mechanism for pressure joining is the film theory (Mohamed *et al.,* 1975; Bay *et al.,* 1979). Metal surfaces are covered with oxide layers, which prohibit metallic bonding between two contacting surfaces. During pressure joining, metals are compressed against each other and deformed, forming many micro-cracks on the surface as the surface oxides break. The virgin metals are then extruded through these micro-cracks and contact the metals on the other surface until a metallic bond is established at the interface. Thus, pressure joining establishes atom-to-atom bonds

between two clean and intimately contacting metallic surfaces under pressure without the formation of a liquid phase (Sahin *et al.,* 2012).

In pressure joining, the joint strength is significantly affected by the amount of deformation and the joining temperature. Plastic deformation is generally necessary to obtain a permanent joint. Mahabunphachai *et al.* (2009) found that threshold and optimal values of deformation exist in pressure joining. Temperature also greatly influences joint performance. Some metal alloys, such as aluminum and copper alloys (Ozel *et al.,* 2005), can be joined successfully at ambient temperature. However, others such as stainless steel, magnesium alloys, and titanium alloys can only be joined at elevated temperatures. Somekawa *et al*. (2003) successfully joined commercial magnesium AZ31 alloys at temperatures between 623 K to 723 K by selecting the appropriate pressure and time. Mahabunphachai *et al*. (2009) found that stainless steel blanks could not be joined when the temperature was below 150℃. It has also been reported that with increasing temperature, the threshold deformation required for joint formation decreases and the joint strength increases (Eizadjou *et al.,* 2008; Eizadjou *et al.,* 2009)).

In conventional pressure joining, the workpiece temperature is usually increased in a furnace. However, this heating method inevitably heats up regions which do not need heating, and requires complex heating and control facilities. To overcome such drawbacks, electrically assisted pressure joining (EAPJ) was suggested to raise the temperature of the metals by resistance heating (Peng *et al.,* 2014). Researchers have successfully demonstrated this process on sheet metals and foils. For example, Ng *et al.* (2015) successfully joined aluminum and copper sheets using an electrically-assisted roll bonding process, and Xu *et al.* (2014) joined stainless steel 316L foils using EAPJ.

Unfortunately, studies on EAPJ of metal alloys are still limited and are mostly conducted on very thin foils. In the present study, lap joints of 1 mm thick Grade 1 Ti alloy sheets were fabricated by EAPJ. The suitability of EAPJ for the selected Ti alloy was evaluated along with the effects of joining parameters on the joint performance to provide guidance for process optimization.

2.2 Experimental set-up

Grade 1 Ti alloy sheets with a thickness of 1 mm were used for the experiment. The nominal chemical compositions of the alloy are listed in Table 2.1. Joining specimens with a length of 120 mm and a width of 10 mm were fabricated by laser cutting along the rolling direction of the as-received Grade 1 Ti sheets, as shown in Figure 2.1(a). Prior to the experiment, the specimens were degreased with acetone to remove oil from the surface. For EAPJ, a custom-made fixture was designed (Figure 2.1(b)) and installed in a universal testing machine (DTU-900MH, Daekyoung, South Korea). Upper and lower dies with small tips of carbon steel with a hardness of HRC > 60 were used as electrodes. The end face of the tip was semicircular with a radius of 2 mm, as shown in the inset of Figure 2.1(b).

During the joining process, a preload of 100 N was applied to the specimens by the universal testing machine to ensure good contact between the dies (electrodes) and the specimens and to avoid sparks between them. Then, axial compression with a constant displacement rate of 12 mm/min and a continuous electric current with a duration of 10 sec were applied to the specimens simultaneously, as listed in Table 2.2 and schematically described in Figure 2.2. As listed in Table 2.2, each magnitude of electric current (current

intensity) corresponded to four or six different maximum displacements. To verify the repeatability of these results, at least three specimens were tested for each parameter set.

Table 2.1 The nominal chemical compositions of Grade 1 Ti alloy.

Alloying element, wt%	Ti	C	Fe	H	N	O
	At balance	≤0.1	≤0.2	≤0.015	≤0.03	≤0.18

120 mm

40 mm

10 mm

Upper sheet

Lower sheet

Joining line

(a)

Universal testing machine

Insulator

Die (as electrode)

⊕

IR camera

Specimens

V

Die (as electrode)

⊖

Insulator

Die (electrode)

R2

DAQ
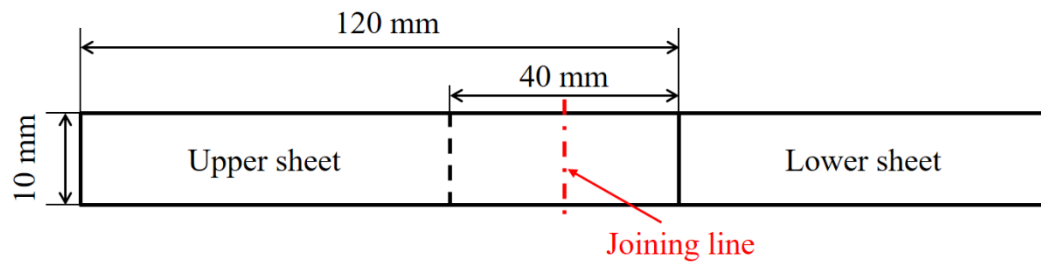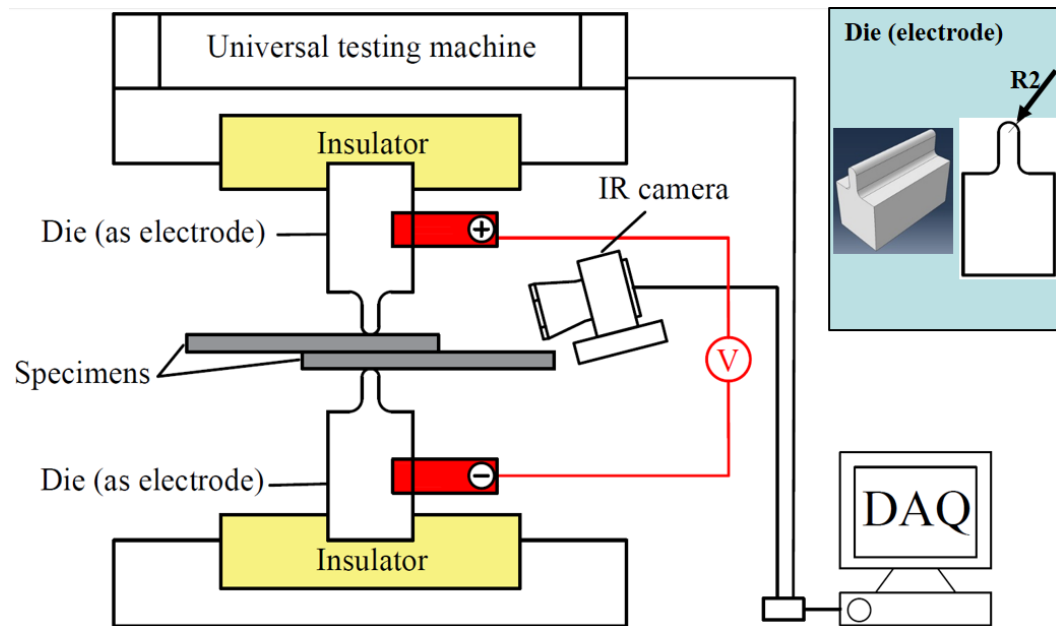
(b)

Figure 2.1 (a) Configuration of joints and dimensions of specimens and (b) Schematic of the

experimental set-up.

Table 2.2 Parameters of EAPJ experiment.

Current intensity (kA)	Maximum displacement (mm)	Thickness reduction (R_t) (%)
1.2	1.3	43.0
	1.4	48.5
	1.5	51.8
	1.7	62.7
	1.9	68.5
	2.0	71.0
1.4	0.9	43.2
	1.0	47.0
	1.1	50.5
	1.3	57.7
	1.5	67.2
	1.6	72.5
1.6	0.7	39.7
	0.9	53.2
	1.1	62.3
	1.3	69.0
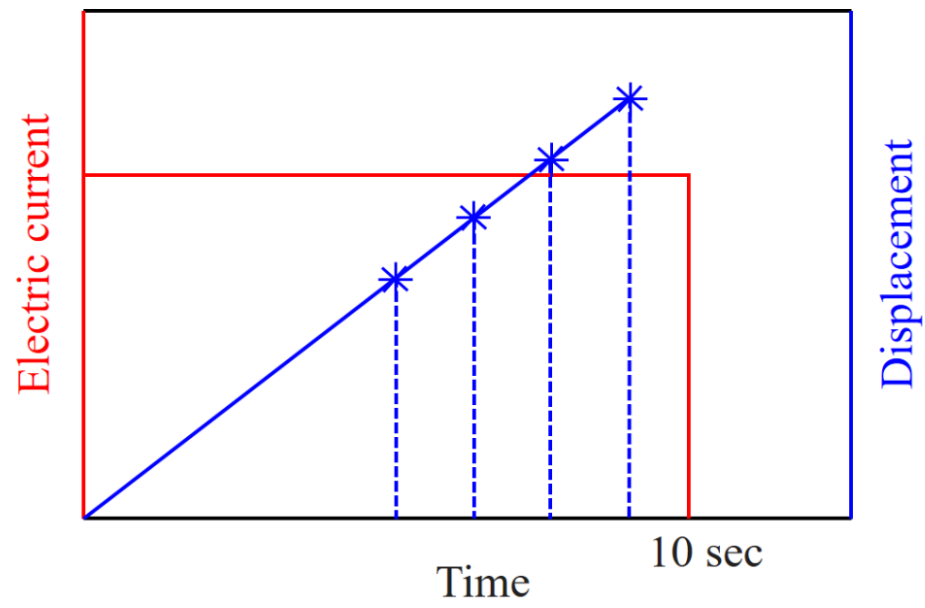
Figure 2.2 Schematic of electric current and displacement during EAPJ.

The load history during EAPJ was measured by a load cell and recorded as a function of displacement using a PC-based data acquisition system. Resistance heating for joining was induced by an electric current generator (Vadal SP-1000U, Hyosung, South Korea) with a programmable controller. Also, a set of insulators made of bakelite was inserted between the dies and the machine to isolate the electricity from the testing equipment. A fusion welding process, resistance spot welding (RSW) with a spot size of 6 mm, was also conducted on the same specimen configuration in a control group (Figure 2.1(a)). An infrared thermal imaging camera (FLIR-T621, FILR, Sweden) was employed to monitor the temperature of the specimens during joining.

Microstructural analysis was conducted on the cross section of the joint perpendicular to the width. The cross section was first etched with Kroll's reagent and examined by optical microscopy (OM) to confirm that the joint contained no macroscopic defects. The microstructure of the joint was further observed using a field emission gun scanning electron microscope (FE-SEM, SU70, Hitachi, Japan) equipped with an electron backscatter diffraction system (EBSD, EDAX/TSL, Hikari, USA). The grain boundaries were defined as a misorientation angle of $15°$. Vickers hardness measurements (300 gf, 10 sec) were also carried out on the cross section perpendicular to the width using a Vickers indenter (HM-100, Mitutoyo, Japan).

The mechanical properties of the joints were evaluated by lap shear tensile tests (Figure 2.3(a)) with a displacement rate of 1 mm/min. To align the direction of force along the center of the joint, a spacer was placed on each sheet.

2.3 Results and discussion

For convenience of analysis, each joint was labeled according to the combination of the current intensity and the maximum displacement applied to it. For example, the 1.2kA1.3d joint represents the joint fabricated using the current intensity of 1.2 kA and the maximum displacement of 1.3 mm. Typical joints produced by EAPJ with different parameters are shown in Figure 2.3(b). Obvious indentation marks are visible on all of the joints. A color change due to high-temperature oxidation was clearly observed in the 1.6kA1.3d joint. Three different parameters, 1.2kA1.9d, 1.4kA1.5d and 1.6kA1.3d, were selected to make comparison on the load and temperature histories due to similar thickness reduction, as shown in Figure 2.4. The load histories during EAPJ (Figure 2.4(a)) show that the compressive load decreased as current intensity increased. Also, the maximum temperature histories (Figure 2.4(b)) show that the maximum temperature increased as current intensity increased due to higher resistance heating.

Spacer

F ← ⋯ → F

Spacer

(a)

1·2 kA 1·3 d

1·4 kA 1·3 d

1·6 kA 1·3 d

10 mm
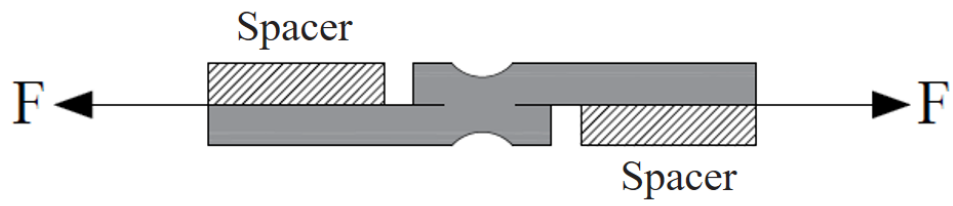
(b)

Figure 2.3 (a) Schematic of lap shear tensile test and (b) appearance of EAPJ joints.
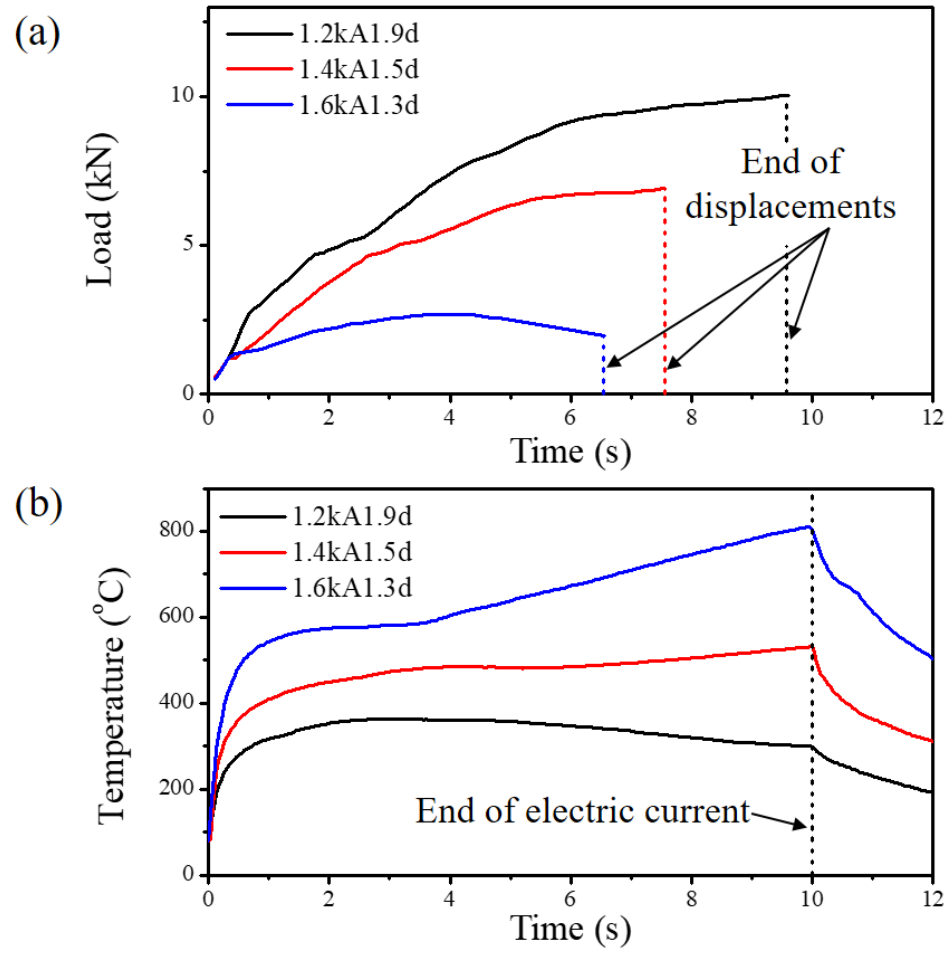
Figure 2.4 (a) Load and (b) maximum temperature histories during EAPJ.

The OM image of the base metal shows a homogeneously equiaxed structure (Figure 2.5(a)). As expected, significant coarse columnar grains perpendicular to the joint interface (approximately marked by arrows) were observed in the fusion zone of the RSW joint (Figure 2.5(b)) due to the prevailing thermal conditions during metal solidification. Much finer grains were observed in the EAPJ joints than in the RSW joint across the joint interface (approximately marked by arrows), as shown in Figures 2.5(c) and (d). The sound joining was obtained for all specimens from both macroscopic and microscopic points of view. Note that severely deformed grains were observed in a region near the joint interface in the 1.2kA1.9d joint (Figure 2.5(c)). The 1.6kA0.7d joint, which experienced the highest current intensity and maximum temperature during EAPJ, has coarser grains comparing with the base metal and the 1.2kA1.9d joint. This suggests that the microstructural change during EAPJ such as recrystallization and grain growth strongly depends on the selected joining parameters.

EBSD inverse pole figure maps (normal direction) and the Kernel average misorientation (KAM) maps on the cross section perpendicular to joint interface are presented in Figure 2.6. In the base metal (Figure 2.6(a)), the microstructure observed in EBSD showed the same tendency as the OM. The average grain size was 38.72 ± 17.05 μm and a strong (0001) basal texture was developed. In the case of the 1.6kA0.7d joint (Figure 2.6(c)), which experienced the highest maximum temperature during EAPJ, had coarser grains (average grain size of 66.96 ± 35.41 μm) than the base metal. This suggests that grain growth after recrystallization during EAPJ was significant for the joining parameters selected in the present study. Once again, microstructural continuity was visible across the joint interface (approximately marked by arrows). The (0001) basal texture was not found in

the 1.6kA0.7d joint. Also, KAM analysis was performed to evaluate the degree of dislocation density. As shown in Figure 2.6(b), very fine grains along the shear band were observed due to recrystallization in the 1.4kA1.3d joint. The KAM values in the shear band are quite high due to plastic deformation. Considering that the recrystallization condition of pure Ti is 30 min at 550°C (Yamane *et al.,* 1963), it can be confirmed that a sound solid-state joint was produced by the accelerated atomic diffusion and recrystallization during 1.4kA1.3d EAPJ maintained at only 520°C for 10 sec (Kim *et al.,* 2014; Kim *et al.,* 2017; Park *et al.,* 2017). The 1.6kA0.7d joint, which experienced the highest current intensity during EAPJ, had coarser grains and lower KAM value comparing with the 1.4kA1.3d joint. This implies that the grains grew during EAPJ.
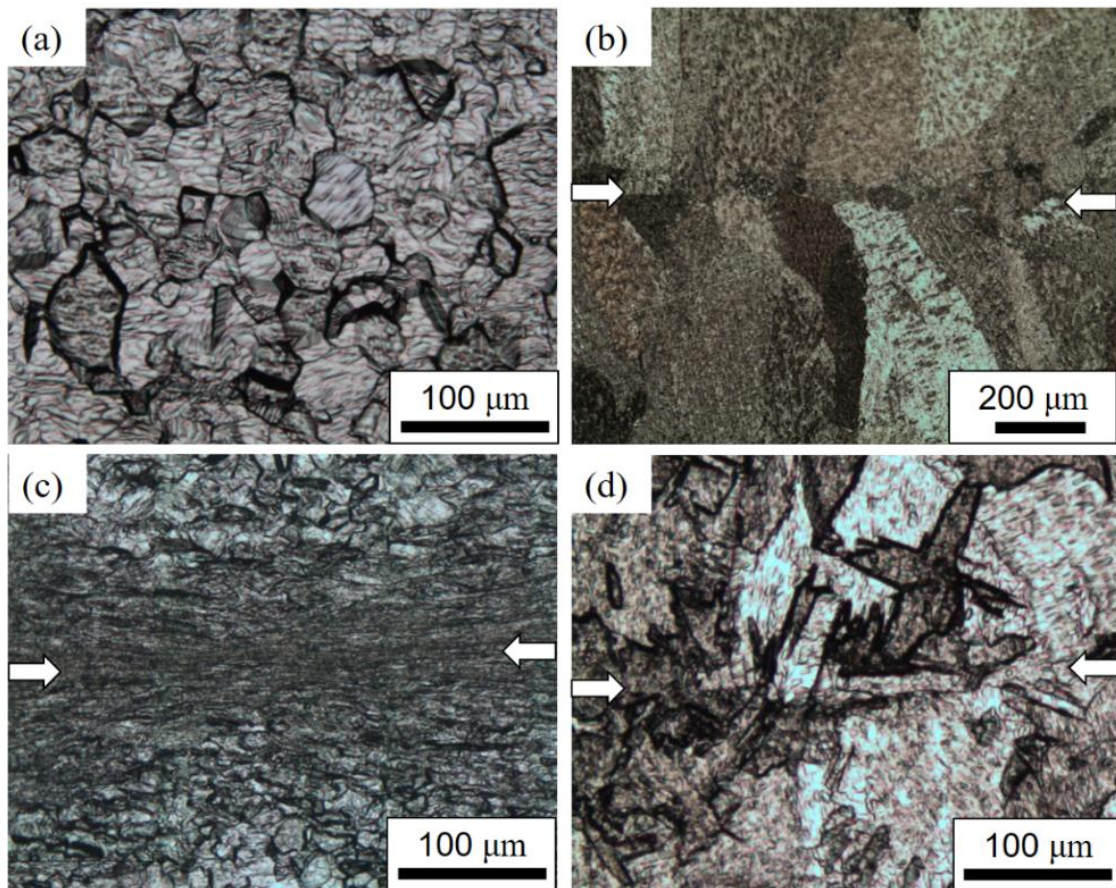
Figure 2.5 OM images of (a) base metal, (b) RSW joint, (c) 1.2kA1.9d joint, and (d)

1.6kA0.7d joint.
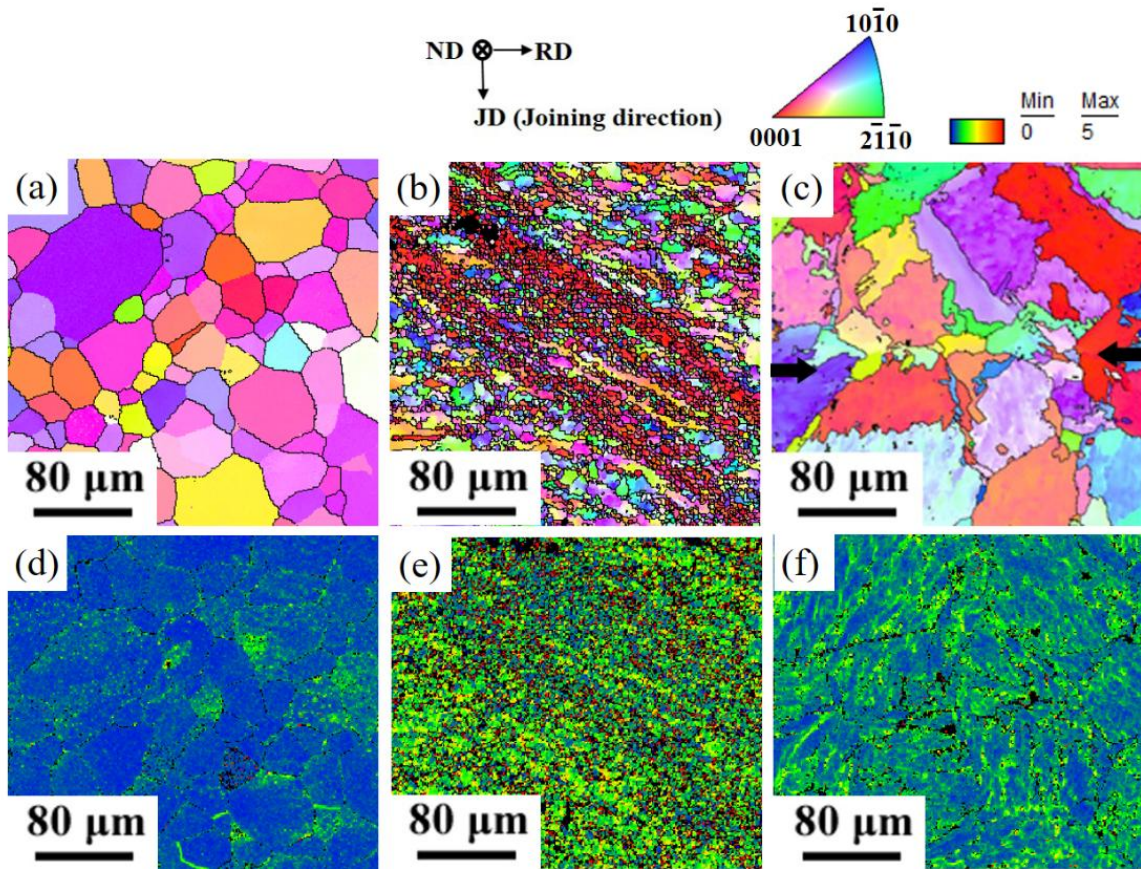
Figure 2.6 EBSD inverse pole figure maps (ND) of (a) base metal, (b) 1.4kA1.3d joint, and

(c) 1.6kA0.7d joint; KAM maps of (d) base metal, (e) 1.4kA1.3d joint, and (f) 1.6kA0.7d

joint.

The thickness of each joint after unloading was also measured in the present study. The thickness reduction R_t (Table 2.2), which indicates the amount of plastic deformation in the EAPJ joint, was calculated by dividing the reduced thickness after unloading by the original specimen thickness. The relationship between thickness reduction and maximum displacement is shown in Figure 2.7, clearly indicating that at the same maximum displacement, the thickness reduction increases as current intensity increases due to the lower flow stress and lower elastic recovery.

The Vickers microhardness of the cross sections of the 1.2kA1.9d, 1.4kA1.5d, and 1.6kA1.3d joints, which had similar thickness reductions of 68.5%, 67.2%, and 69.0%, respectively, was measured along the center line of the joint region and the smooth transition to base metal (marked by a red dashed line in the inset of Figure 2.8). The hardness of all three joints was significantly higher in the center of the joint region than that of the base metal due to strain hardening by compressive deformation during EAPJ. The hardness in the joint region also generally decreased as the current intensity increased, which suggests that the effect of strain hardening was reduced and electrically induced annealing (Kim *et al.,* 2014; Kim *et al.,* 2017; Park *et al.,* 2017) was enhanced by the higher current intensity and the higher joining temperature.
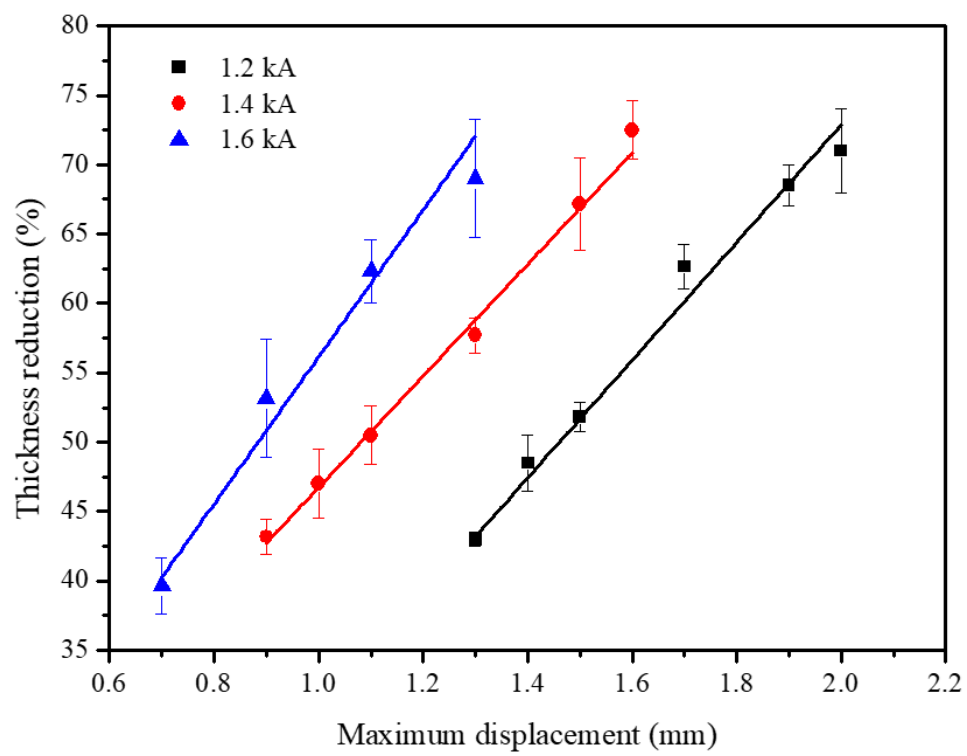
Figure 2.7 Relationship between thickness reduction and maximum displacement.
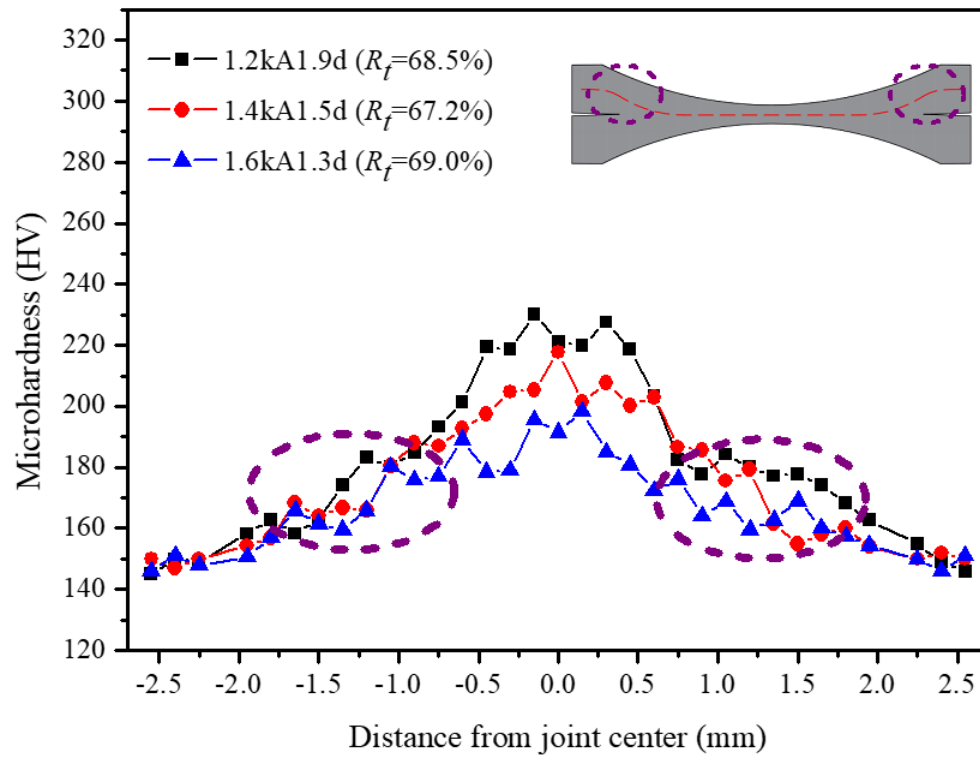
Figure 2.8 Microhardness profiles of joints.

Two different fracture modes (shear fracture and tensile fracture) were observed in lap shear tensile tests of the EAPJ joints. In the shear fracture mode, fracture occurred across the joint interface (interface separation), as schematically shown in Figure 2.9(a). In the tensile fracture mode, fracture occurred on one sheet metal along the edge of the joint, as schematically shown in Figure 2.9(a). Figures 2.9(b) and (c) show specimens fractured by the shear fracture mode and the tensile fracture mode, respectively. Note that when the thickness reduction was excessive (greater than ~75%) fracture simply occurred in the middle of the joint. This fracture mode is not considered in the present study due to low joint strength.

The relationship between fracture load and thickness reduction with different EAPJ parameter combinations shows that electric current and thickness reduction have a significant effect on the mechanical behavior of an EAPJ joint (Figure 2.10). For the current intensities of 1.2 kA and 1.4 kA, both fracture modes were observed. Shear fracture occurred when the thickness reduction was relatively small. For a given current intensity, the shear fracture load increased with increasing thickness reduction. Also, for similar values of thickness reduction, a higher current intensity resulted in a higher shear fracture load. These results can be simply explained by the effects of thickness reduction and current intensity on the joint length and shear strength of the joint (or simply the joint shear strength). As listed in Table 2.3, with increasing thickness reduction or current intensity, both the joint length and the joint shear strength increased since the diffusion at the interface was enhanced.
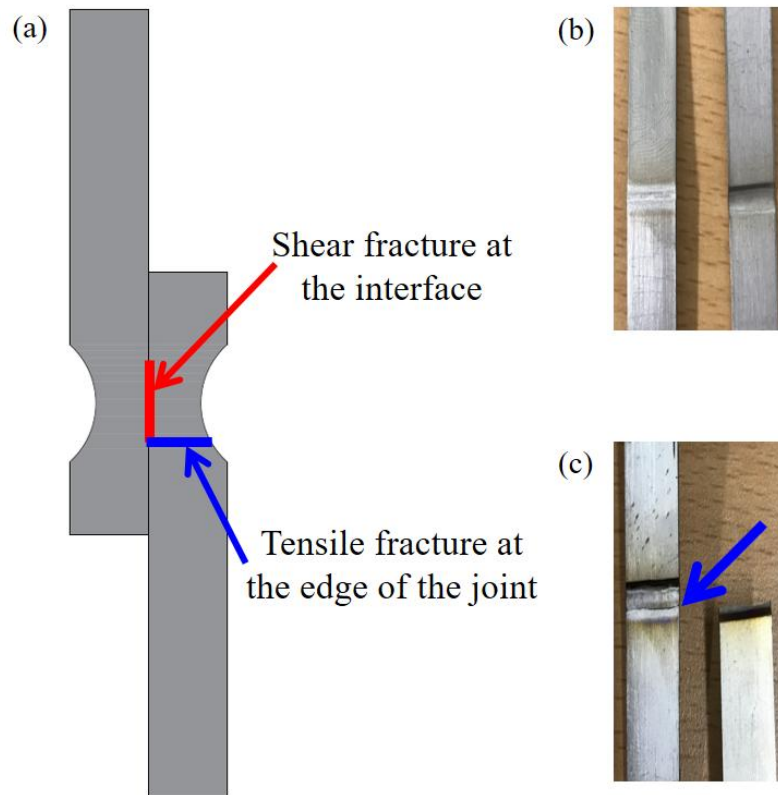
Figure 2.9 (a) Schematic of fracture modes; EAPJ joints fractured by (b) shear fracture mode

and (c) tensile fracture mode.
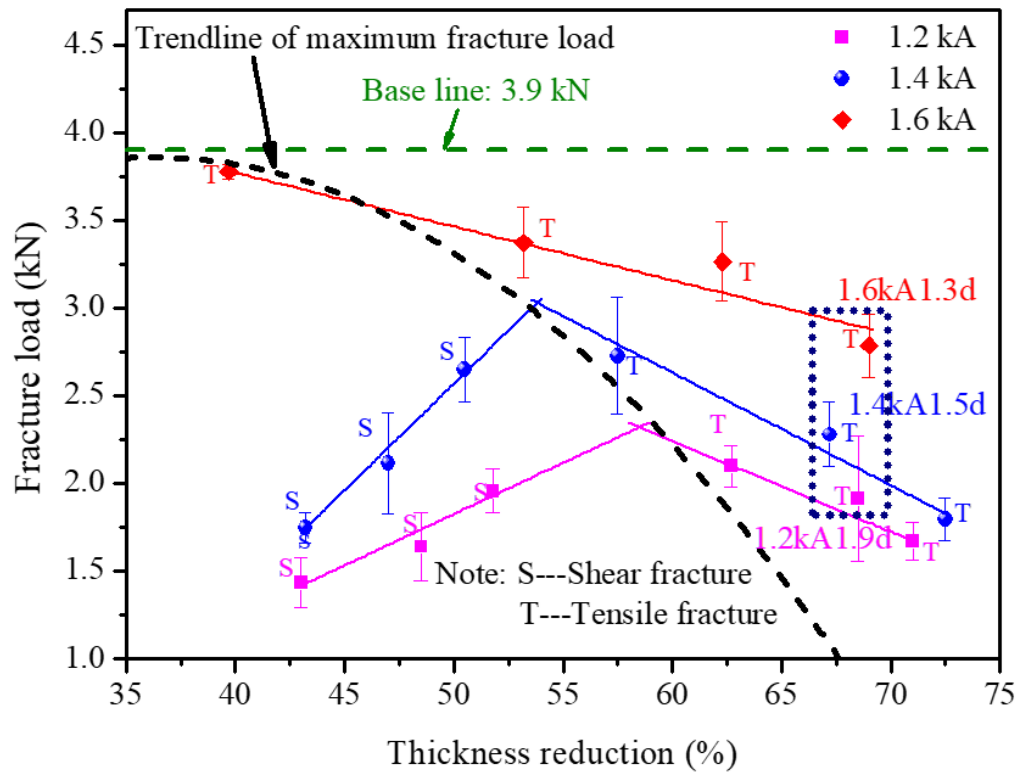
Figure 2.10 Fracture load as a function of thickness reduction for different EAPJ parameter

combinations.

Table 2.3 Joint properties with the current intensities of 1.2 kA and 1.4 kA in shear fracture mode.

Joint	Joint length (mm)	Thickness reduction (%)	Shear fracture load (N)	Average shear strength (MPa)
1.2kA1.3d	0.734±0.061	43.0±0.5	1437±138	195.78
1.2kA1.4d	0.827±0.055	48.5±2.0	1640±194	198.30
1.2kA1.5d	0.969±0.068	51.8±1.0	1958±127	202.06
1.4kA0.9d	0.815±0.082	43.2±1.3	1748±85	214.48
1.4kA1.0d	0.967±0.091	47.0±2.5	2117±289	218.92
1.4kA1.1d	1.150±0.024	50.5±2.1	2649±184	230.35

For the current intensities of 1.2 kA and 1.4 kA, the tensile fracture mode began to occur when the thickness reduction exceeded a critical value. This transition of fracture mode from shear to tensile can be explained using the relative magnitudes of the shear fracture load and the tensile fracture load. When the thickness reduction is low, the tensile fracture load is sufficiently larger than the shear fracture load due to large thickness in the tensile fracture region. However, as the thickness reduction increases, the shear fracture load increases with the increases in joint length and joint shear strength, while the tensile fracture load decreases due to the reduction of the thickness in the tensile fracture region (marked by a blue line in Figure 2.9(a)). Once the increasing shear fracture load exceeds the decreasing tensile fracture load, the tensile fracture mode becomes the dominant fracture mode of the joint. At the current intensity of 1.6 kA, the joint shear strength greatly improved and only the tensile fracture mode was visible, as shown in Figure 2.10. Note that the maximum tensile fracture load of about 3.78 kN (96% of that of the base metal) was achieved in the 1.6kA0.7d joint. Also, the steady decrease in tensile fracture load with increasing thickness reduction for all three current intensities suggests that the effect of thickness reduction on the tensile fracture load (corresponding to reduced tensile fracture thickness) surpassed that of strain hardening for the experimental conditions considered in the present study.

Note that in the tensile fracture mode region, the fracture load also increased with increasing current intensity for values of similar thickness reduction, as marked by a dashed box in Figure 2.10. The hardnesses of these three joints in the joint edge region (tensile fracture region) were only slightly different, as shown in Figure 2.8. Therefore, the mechanical strength of the three joint edge regions should be similar. The increase in tensile fracture load with increasing current intensity can be explained quite simply by the

geometric effect. As mentioned earlier, with similar thickness reduction, the joint length increases as the current intensity increases. Naturally, the increase in joint length changes the location of the joint edge and consequently increases the tensile fracture thickness, as shown in Figures 2.11(a) and (b).

The trend line of maximum fracture load for each current intensity can be approximated as shown in Figure 2.10. The trend line, which is the dividing line between the shear fracture and tensile fracture modes, suggests that higher joint strength can be obtained by a higher current intensity with lower thickness reduction. Of course, it should be noted that an excessively high current intensity with low thickness reduction would simply result in resistance welding (RW) or RSW, which is a conventional fusion joining process and would nullify the benefits of solid-state joining.

Based on the results shown in Figure 2.10, the optimal thickness reduction, which corresponds to the maximum fracture load for a given current intensity, can be plotted as a function of current intensity. As shown in Figure 2.12, the optimal thickness reduction decreases as the current intensity increases. An empirical relation between the optimal thickness reduction (R_t) and current intensity (I_A) can be written as a quadratic function as follows:

$$0.28(I_A)^2 + 1.73(R_t)^2 = 1 \tag{2.1}$$

where 0.28 and 1.73 are parameters that depend on the material properties and the shape of the electrode tips (dies). The current intensity I_A can be converted into a current density using the geometry of the electrode tip and the dimensions of the specimen. To confirm the validity of the empirical relation suggested in Figure 2.12 and Eqn. (2.1), a set of additional validation experiments with the current intensity of 1.3 kA was conducted. As

shown in Figure 2.12, the result of the validation experiments (a hollow symbol) corresponds quite well with the empirical relation based on the results of the original experiments (solid symbols). The empirical relation between R_t and I_A provides a design guide for EAPJ of a given Ti alloy.
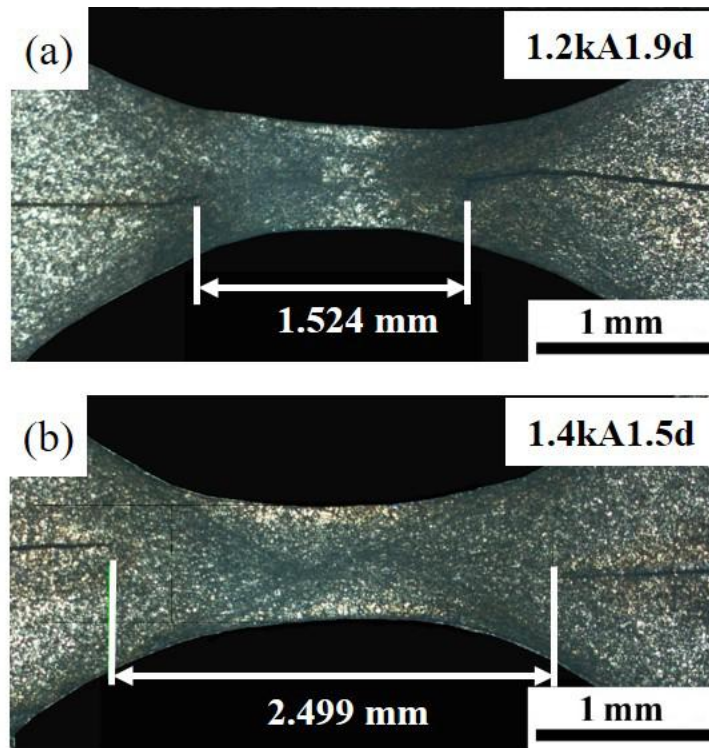
Figure 2.11 Cross-sectional macrographs of (a) 1.2kA1.9d and (b) 1.4kA1.5d joints.
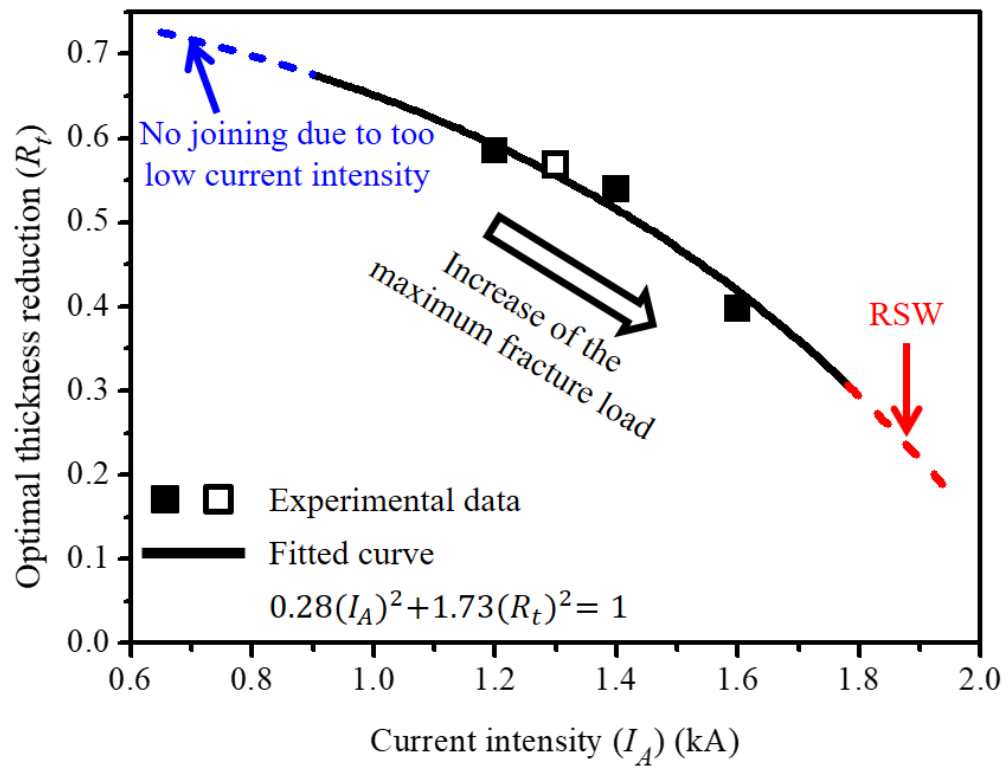
Figure 2.12 Optimal thickness reduction as a function of current intensity; The hollow symbol represents the result of validation experiments after the construction of the empirical relation.

2.4 Conclusion

In the present study, 1 mm thick Grade 1 Ti alloy sheets were successfully joined by EAPJ at temperatures significantly lower than the melting temperature of the alloy. The results of OM and EBSD analysis confirmed that a sound solid-state joint was successfully fabricated by EAPJ due to the diffusion of atoms and recrystallization under the combined action of electric current and compression. The joining load (or thickness reduction) needed for EAPJ can be reduced rapidly by increasing current intensity. The lap shear tensile tests showed that thickness reduction and current intensity have significant effects on the mechanical behavior of the joint. An optimal thickness reduction, corresponding to the maximum fracture load, exists for each value of current intensity, and decreases as current intensity increases. A higher fracture load can be obtained by adjusting the combination of the current intensity and the thickness reduction parameters. The results of the present study provide a design guide for the optimization of lap joining by EAPJ.

References

Baudana G, Biamino S, Ugues D, Lombardi M, Fino P, Pavese M, Badini C (2016) Titanium aluminides for aerospace and automotive applications processed by electron beam melting: contribution of politecnico di torino. Metal Powder Report 71(3):193-199.

Bay N (1979) Cold pressure welding-the mechanisms governing bonding. Journal of Engineering for Industry 101(2):121-127.

Eizadjou M, Danesh Manesh H, Janghorban K (2008) Investigation of roll bonding between aluminum alloy strips. Materials & Design 29(4):909-913.

Eizadjou M, Danesh Manesh H, Janghorban K (2009) Mechanism of warm and cold roll bonding of aluminum alloy strips. Materials & Design 30(10):4156-4161.

Fujii H, Sun Y, Kato H, Nakata K (2010) Investigation of welding parameter dependent microstructure and mechanical properties in friction stir welded pure Ti joints. Materials Science and Engineering: A 527(15):3386-91.

Kim MJ, Lee K, Oh KH, Choi IS, Yu HH, Hong ST, Han HN (2014) Electric current-induced annealing during uniaxial tension of aluminum alloy. Scripta Materialia 75(15):58-61.

Kim MJ, Lee MG, Hariharan K, Hong ST, Choi IS, Kim D, Oh KH, Han HN (2017) Electric current-assisted deformation behavior of Al-Mg-Si alloy under uniaxial tension. International Journal of Plasticity 94:148-170.

Lathabai S, Jarvis BL, Barton KJ (2001) Comparison of keyhole and conventional gas tungsten arc welds in commercially pure titanium. Materials Science and Engineering: A 299(1-2):81-93.

Lee WB, Lee CY, Chang WS, Yeon YM, Jung SB (2005) Microstructural investigation of friction stir welded pure titanium. Materials Letters 59(26):3315-3318.

Mahabunphachai S, Koç M, Ni J (2009) Pressure welding of thin sheet metals: experimental investigations and analytical modeling. Journal of Manufacturing Science and Engineering 131(4):041003(1)-(9).

Mohamed HA, Washburn J (1975) Mechanism of solid state pressure welding. Weld Journal :302-310.

Mohammed MT (2017) Development of a new metastable beta titanium alloy for biomedical applications. Karbala International Journal of Modern Science 3(4):224-230.

Ng MK, Li L, Fan Z, Gao RX, Smith III EF, Ehmann KF, Cao J (2015) Joining sheet metals by electrically-assisted roll bonding. CIRP Annals Manufacturing Technology 64(1):273-276.

Ozel K, Sahin M, Akdogan A (2005) Mechanical and metallurgical properties of aluminium and copper sheets joined by cold pressure welding. Journal Mechanical Engineering 54(11):796-806.

Park JW, Jeong HJ, Jin SW, Kim MJ, Lee K, Kim JJ, Hong ST, Han HN (2017) Effect of electric current on recrystallization kinetics in interstitial free steel and AZ31 magnesium alloy. Materials Characterization 133:70-76.

Peng L, Xu Z, Lai X (2014) An investigation of electrical-assisted solid-state welding/bonding process for thin metallic sheets: experiments and modeling. Proceedings of the Institution of Mechanical Engineers Part B Journal of Engineering Manufacture 228(4):582-594.

Sahin M, Misirli C (2012) Properties of cold pressure welded aluminium and copper sheets. Advanced Materials Research 463-464:244-248.

Saresh N, Gopalakrishna Pillai M, Mathew J (2007) Investigations into the effects of electron beam welding on thick Ti-6Al-4V titanium alloy. Journal of Materials Processing Technology 192-193:83-88.

Somekawa H, Hosokawa H, Watanabe H, Higashi K (2003) Diffusion bonding in superplastic magnesium alloys. Materials Science and Engineering: A 339(1-2):328-333.

Xu Z, Peng L, Lai X (2014) Electrically assisted solid-state pressure welding process of SS 316 sheet metals. Journal of Materials Processing Technology 214(11):2212-2219.

Yamane T, Ueda J (1963) Recrystallization of a cold rolled commercial pure titanium plate by isothermal annealing. Transactions and Japan Institute of Metals 4:242-245.

CHAPTER Ⅲ

EFFECTIVENESS OF ELECTRICALLY ASSISTED SOLID-STATE PRESSURE JOINING USING AN ADDITIVE MANUFACTURED POROUS INTERLAYER

ABSTRACT

A solid-state pressure joining using resistance heating as a heat source and adopting an additive manufactured metal porous interlayer between joining specimens is demonstrated. During the joining of 316L stainless steel cylindrical specimens, an electric current is directly applied to the joint under continuous axial compression. Defect-free joints are successfully fabricated with a lower joining pressure when applying the porous interlayer with a lower compressive strength and higher electric resistivity. The microstructural analysis confirms that the porosity is eliminated as a result of the compressive deformation during joining, and recrystallization takes place in the interlayer.

Keywords: Joining; Additive manufacturing; Porous interlayer

3.1 Introduction

In the manufacture of metallic structural components, joining is an inevitable process due to the limited formability of metal alloys. In the joining of metallic components, fusion joining due to the melting and solidification of metals is commonly employed. However, with increasing use of dissimilar or difficult-to-weld metal alloys, the number of occasions in which conventional fusion joining is not applicable has been increasing in various industries.

Various solid-state joining processes, which are metallurgical joining processes by plastic deformation (Mori *et al.,* 2013), have been considered as alternatives for conventional fusion joining processes. Except for friction stir welding (Meshram *et al.,* 2014; Zheng *et al.,* 2016; Hong *et al.,* 2017), which generates a solid-state joint resulting from the mechanical stirring of metals using a rotating tool, solid-state joining processes such as pressure joining (Monamed *et al.,* 1975; Zhang *et al.,* 1997) and friction welding (Kimura *et al.,* 2017; Sarsilmaza *et al.,* 2017) generally generate joints by establishing diffusion bonding between metal surfaces under pressure. In pressure joining, metals are compressed against each other and deformed. Due to the compressive deformation of metals, the oxide layers, which prohibit metallurgical bonding of the metal surfaces in contact, break and virgin metals make contact with each other (Ng *et al.,* 2015; Mahabunphachai *et al.,* 2009). As a result, a solid-state joint is generated without the formation of a liquid phase. In pressure joining, the bond strength is significantly affected by the joining temperature. Even though several metal alloys such as copper, aluminum, and nickel alloys may be successfully joined at ambient temperature (Sahin *et al.,* 2012; Ozel *et al.,* 2008), pressure joining generally needs to be conducted at elevated temperatures. Therefore, in a

49

conventional hot pressure joining process, complex heating and control facilities are generally required. Also, the acceptable size of any part involved in this process is limited to the size of the furnace.

Friction welding also uses the same bonding mechanism of pressure joining and is usually considered for joining cylindrical parts. This produces solid-state joints of metals by the frictional heat obtained from a mechanically induced relative sliding motion (in general, by rotation) between the surfaces of two workpieces in contact under pressure (Kimura *et al.,* 2017; Sarsilmaza *et al.,* 2017). An advantage of friction is that operating temperatures are significantly lower than those of conventional fusion joining. In friction welding, a stationary workpiece is pressed against a rotating workpiece to generate the frictional force and the temperature increases at the contact surfaces. When the temperature reaches the target value, the rotation ceases and additional axial compression is rapidly applied to the workpieces until a satisfactory solid-state joint is generated at the contact surfaces. However, friction welding requires a relatively expensive apparatus. In particular, a special complex brake system is needed since the rotation of a workpiece must be stopped completely and rapidly for successful joining (Kimura *et al.,* 2017). Note that no additional frictional heat is generated during the actual generation of a solid-state joint since the rotation ceases prior to the final axial compression during friction welding. Also, a large amount of flash (or burr) is exhausted from the joint interface by the final axial compression during friction joining and thus must be removed after the process (Louw *et al.,* 1974).

To overcome or minimize the drawbacks of conventional pressure joining and friction welding, electrically assisted pressure joining (EAPJ) using resistance heating as a heat source is a possibility (Peng *et al.,* 2014; Harada *et al.,* 2016). In comparison to conventional

pressure joining, using resistance heating as a heat source provides several technical advantages. First, the workpieces can be heated rapidly and locally. As a result, the process time can be reduced and unnecessary thermal effects on the workpiece can be minimized. Also, the joining apparatus can be significantly simpler and more cost-effective, as the need for a heating furnace can be eliminated. In addition, if present, the electroplastic effect of an electric current enhances the mobility and diffusion of interface atoms (Roh *et al.,* 2014), which may improve the mechanical/material properties of the solid-state joint. EAPJ of metal sheets or foils has been successfully demonstrated by several researchers. For example, Ng *et al*. (2015) conducted electrically assisted roll bonding of aluminum and copper sheets. Xu *et al*. (2013) also joined stainless steel 316L foils by EAPJ.

The concept of EAPJ also provides technical advantages over friction welding in the joining of bulk workpieces. By using resistance heating as a heat source, the need for complex rotation and brake systems can be eliminated. Also, since the heating of the interface can be continued during the final axial compression, process optimization is relatively easier. In the present study, improvement of the process effectiveness for the EAPJ of cylindrical bulk components is demonstrated by using an additive manufactured metal porous interlayer.

3.2 Experimental set-up

For electrically assisted pressure joining (EAPJ) of bulk specimens, solid cylindrical specimens with a diameter of 10 mm were machined using a commercial stainless steel 316L alloy (SUS316L). Solid cylindrical specimens with a height of 15 mm were machined for EAPJ without a metal porous interlayer, while solid cylindrical specimens with a height

of 13 mm were machined for EAPJ with a metal porous interlayer. The metal porous interlayers with a diameter of 10 mm and a height of 4 mm were fabricated using SUS316L powder (Sandvik Osprey, UK) by metal additive manufacturing (or simply, metal 3D printing) with selective laser melting. The particle size of the SUS316L powder used is in the range of 15 to 45 μm. A commercial metal 3D printer (MetalSys 150, Winforsys, South Korea) with a laser spot size of 40μm was used to fabricate the metal porous interlayers. The metal porous interlayers were fabricated to have two different porosities of 8 and 12 vol.% (based on the relative density) by adjusting the process parameters (laser power and scan speed) of the additive manufacturing process, as shown in Figure 3.1(a). The cross-sectional macrographs of porous specimens are shown in Figures 3.1(b) and (c). Also, cylindrical porous specimens (8 and 12 vol.% porosities) with a diameter of 10 mm and a height of 15 mm were fabricated by the same additive manufacturing process to measure of the baseline compressive properties. Baseline uniaxial compression tests were also conducted with a displacement rate of 24 mm/min at room temperature. The chemical compositions of the solid and powder SUS316L are quite similar, as listed in Table 3.1. In the present study, three different assemblies of solid specimens and a porous interlayer were evaluated, as schematically described in Figure 3.2. The three different assemblies are identified as S+S, S/3D8%, and S/3D12%. All the specimens were thoroughly cleaned by acetone prior to the experiments.

Table 3.1 The chemical compositions of solid and powder SS 316L alloys.

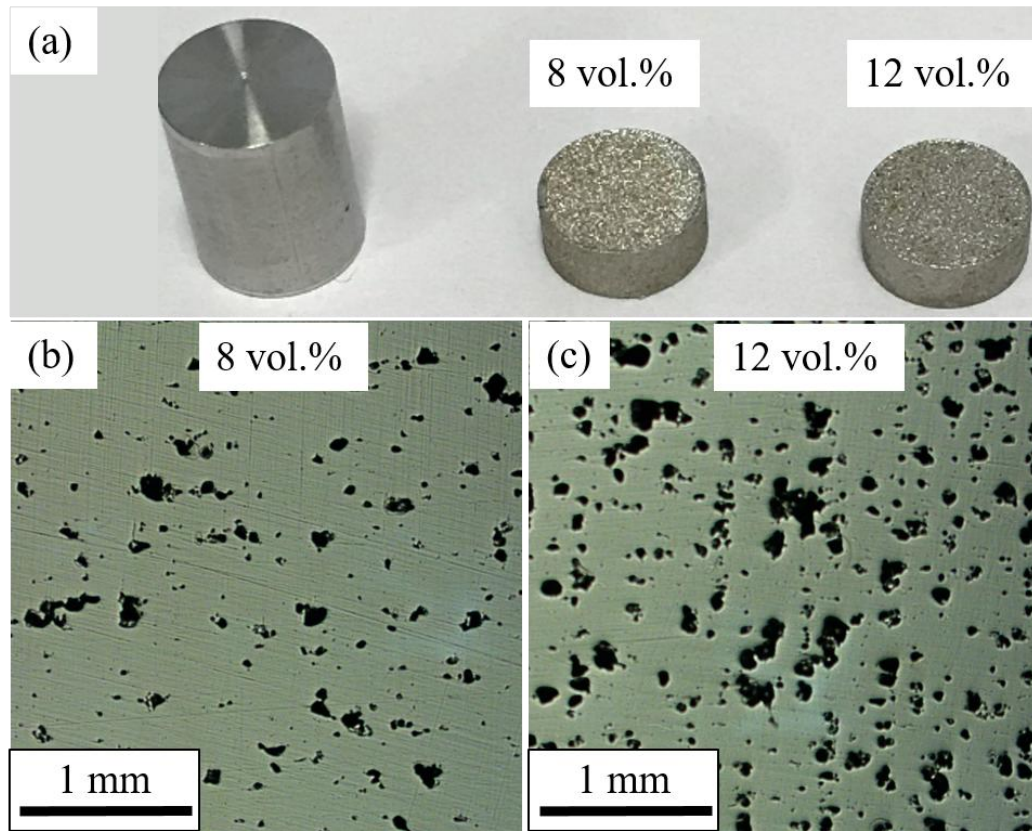|	C	Mn	Si	P	S	Cr	Mo	Ni	N
Solid	≤0.03	≤2.0	≤0.75	≤0.045	≤0.03	≤18.0	≤3.0	≤14.0	≤0.10
Powder	0.018	1.13	0.63	0.02	0.009	17.1	2.3	10.6	---

At balance: Fe

Figure 3.1 (a) Solid specimen and metal porous interlayers, cross-sectional macrographs of metal porous interlayers with porosity of (b) 8 vol.%, and (c) 12 vol.%.
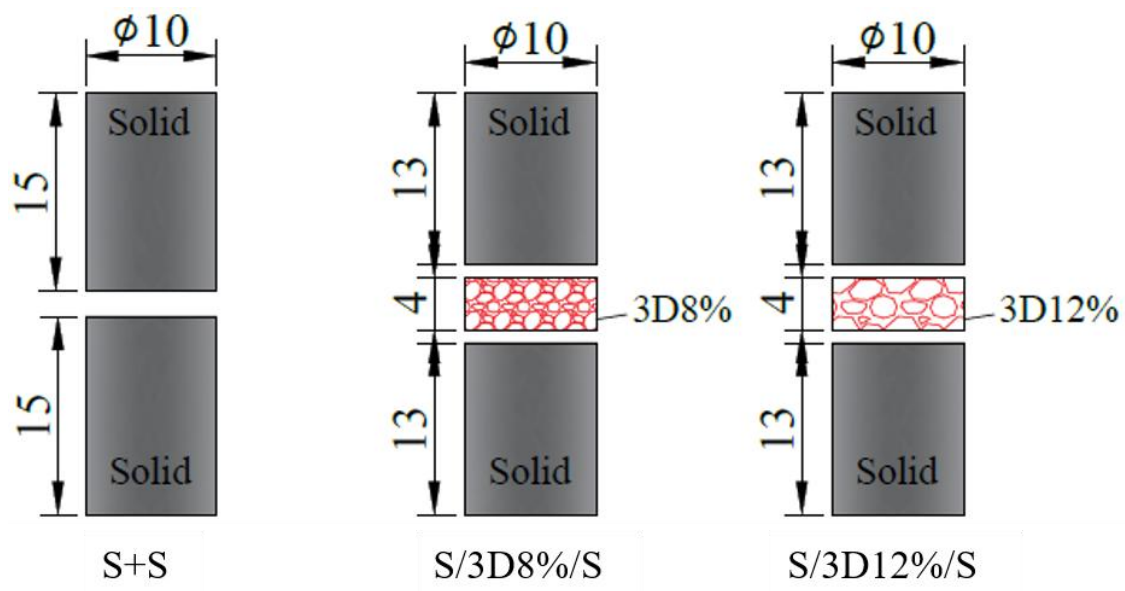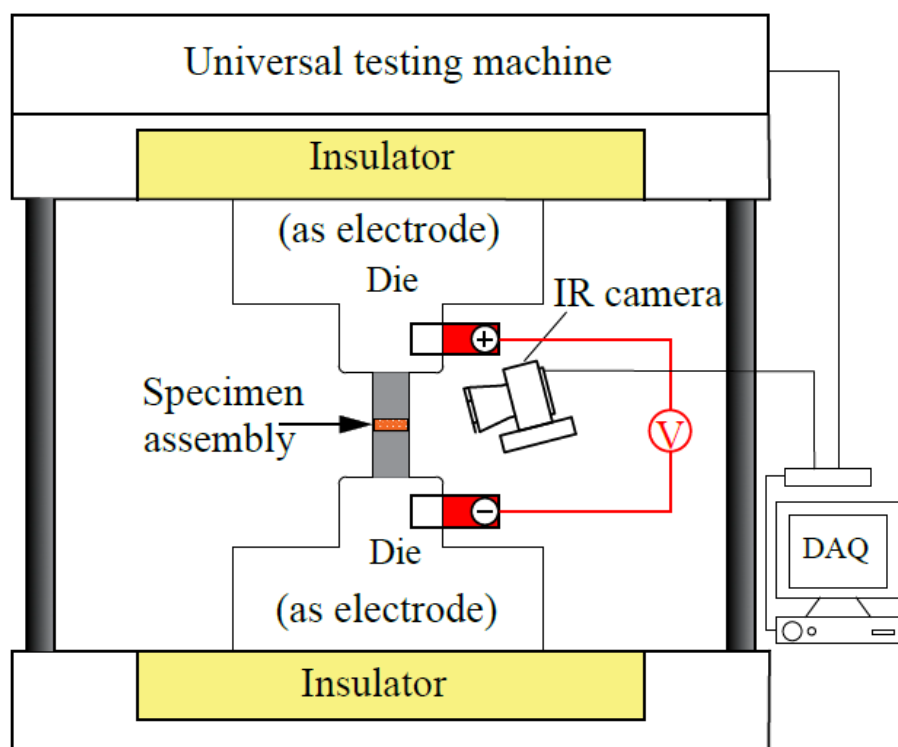
Figure 3.2 Schematic of specimen assemblies.

Figure 3.3 A schematic of the experimental set-up.

A custom-made fixture was installed in a universal testing machine (DTU900-MH, Daekyoung, South Korea) for EAPJ, as schematically shown in Figure 3.3. The resistance heating during compressive deformation for joining was induced by an electric current generator (Vadal SP-1000U, Hyosung, South Korea) with a programmable controller. Upper and lower dies made of tool steel for compression were also used as electrodes. Also, a set of insulators made of bakelite was inserted between the die and the machine to isolate electric current from the testing equipment.

During the EAPJ experiments, a preload of 100 N was applied to the specimen assembly by the universal testing machine to ensure good contact between the electrode (die) and the specimen, thus avoiding sparks or welding between the die and the specimens. Axial compression and an electric current were then simultaneously applied to the specimen assembly, as schematically described in Figure 3.4. In the present study, a constant displacement rate of 24 mm/min and a maximum displacement of 6 mm were used for all EAPJ experiments. As described in Figure 3.4 and listed in Table 3.2, for resistance heating during compression, a continuous electric current was initially applied to the specimen assembly to rapidly increase the temperature of the specimen assembly. Then, a pulsed electric current was applied to the specimen assembly to enhance atomic diffusion by maintaining an elevated temperature without overheating the specimen assembly. To verify the repeatability of the results, the experiments were conducted at least three times for each specimen assembly. In the experiment, the load history was measured by a load cell (CSDH, Bongshin, South Korea) and recorded as a function of displacement using a PC-based data acquisition system. The displacement was measured using an LVDT embedded in the universal testing machine. The temperature of specimen assembly during joining was

continuously monitored and recorded using an infrared thermal imaging camera (FLIR-T621,
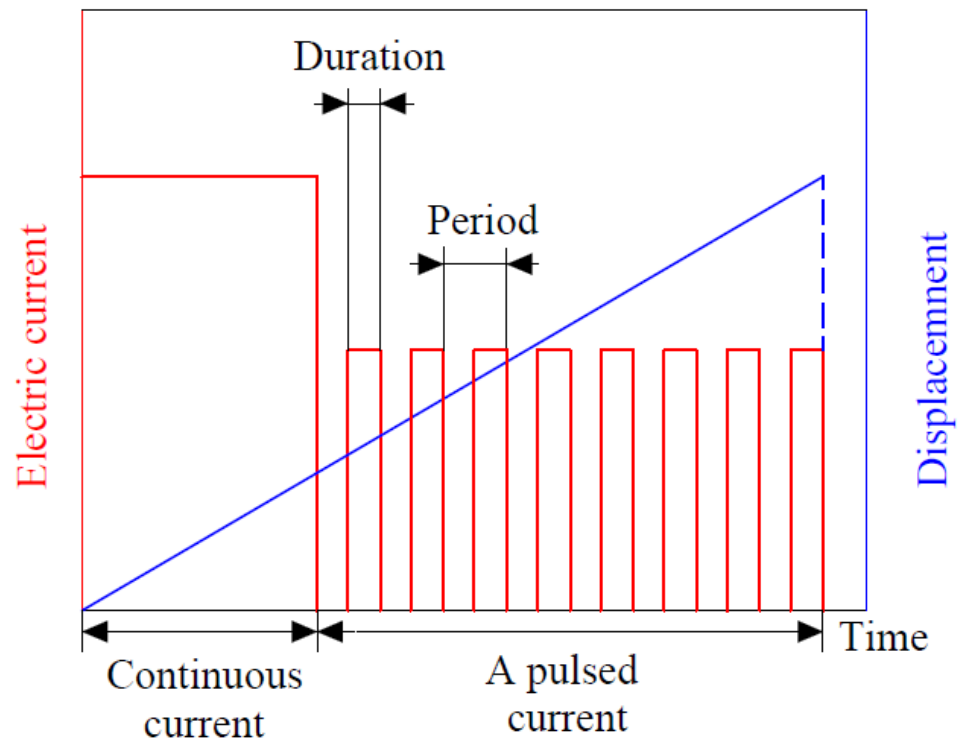
FLIR, Sweden).

Figure 3.4 A schematic of applying electric current during compression process.

Table 3.2 Electric current parameters of joining experiments.

Step	Nominal current density (A/mm^2)	Pulse during (s)	Pulse period (s)	Total time (s)
Continuous current	32	---	---	5
A pulsed current	19	0.75	1.25	10

For the microstructural analysis, the cross section of the joint was prepared along the direction of compression (the height direction). The cross-sectional sample was first examined by optical microscopy (OM) after etching using 50 ml of hydrochloric acid with 15 g of iron (III) chloride to confirm that the joint was fabricated without obvious macroscopic defects. The microstructure of the joint was further observed using a field emission gun scanning electron microscope (FE-SEM, SU70, Hitachi, Japan) equipped with an electron backscatter diffraction system (EBSD, EDAX/TSL, Hikari, USA) and an energy dispersive spectrometer (EDS: X-Max50, Horiba, Japan). The mechanical properties of the joint were evaluated by Vickers hardness measurements (9.8 N,10 sec) of the cross section along the center line in the direction of compression using a Vickers indenter (HM-100, Mitutoyo, Japan). Finally, to confirm a sufficient joint strength, the joints were machined to cylinders with a diameter of 8 mm and simple cantilever bend tests were conducted.

3.3 Results and discussion

The results of the baseline compression test (Figure 3.5) clearly show that the elastic modulus, compressive yield stress, and compressive flow stress of the cylindrical porous specimens fabricated by the additive manufacturing process are lower than those of the solid cylindrical specimen. Note that the load-displacement curve is used instead of the stress-strain curve due to barreling during compression.
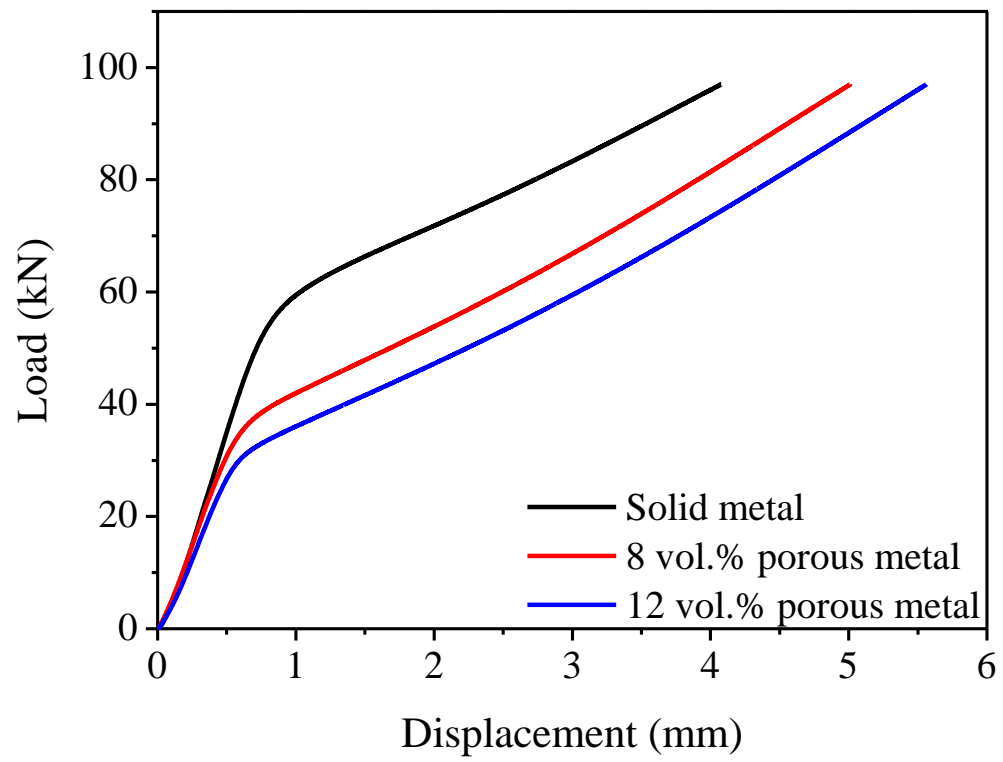
Figure 3.5 Load-displacement curves from the baseline compression tests.

Using the well-known Gibson-Ashby (Gibson *et al.,* 1997) model, the relationship between the relative yield strength and relative density can be described to obey a power law relationship (Gibson *et al.,* 1997; Esen *et al.,* 2007) as,

$$\frac{\sigma_p}{\sigma_s} = 0.90(\frac{\rho_p}{\rho_s})^{4.02} \tag{3.1}$$

where σ and ρ represent the 0.2% compressive yield stress based on the original cross-sectional area and bulk density, respectively. Also, the subscripts *p* and *s* indicate the properties of solid metal and porous metal, respectively. The proportional constant and exponent reflect the porous parameters including the porosity, cell morphology, and arrangement of the cell walls (Gibson *et al.,* 1997; Esen *et al.,* 2007; Dewidar *et al.,* 2007). Note that for the porous specimens considered in the present study, the proportional constant and exponent also reflect the microstructural differences, as the porous specimens were additive manufactured with selective laser melting.

No significant difference in appearance was observed among the EAPJ joints with or without the porous interlayer. For all EAPJ joints, obvious flash formation (or barreling) was observed, as shown in Figure 3.6(a). The diameter measurement results along the height using the 3D laser scanner (AS4500, Abeosystem, South Korea) also confirm that the flash formation is quite similar for all of the EAPJ joints (Figure 3.6(b)).
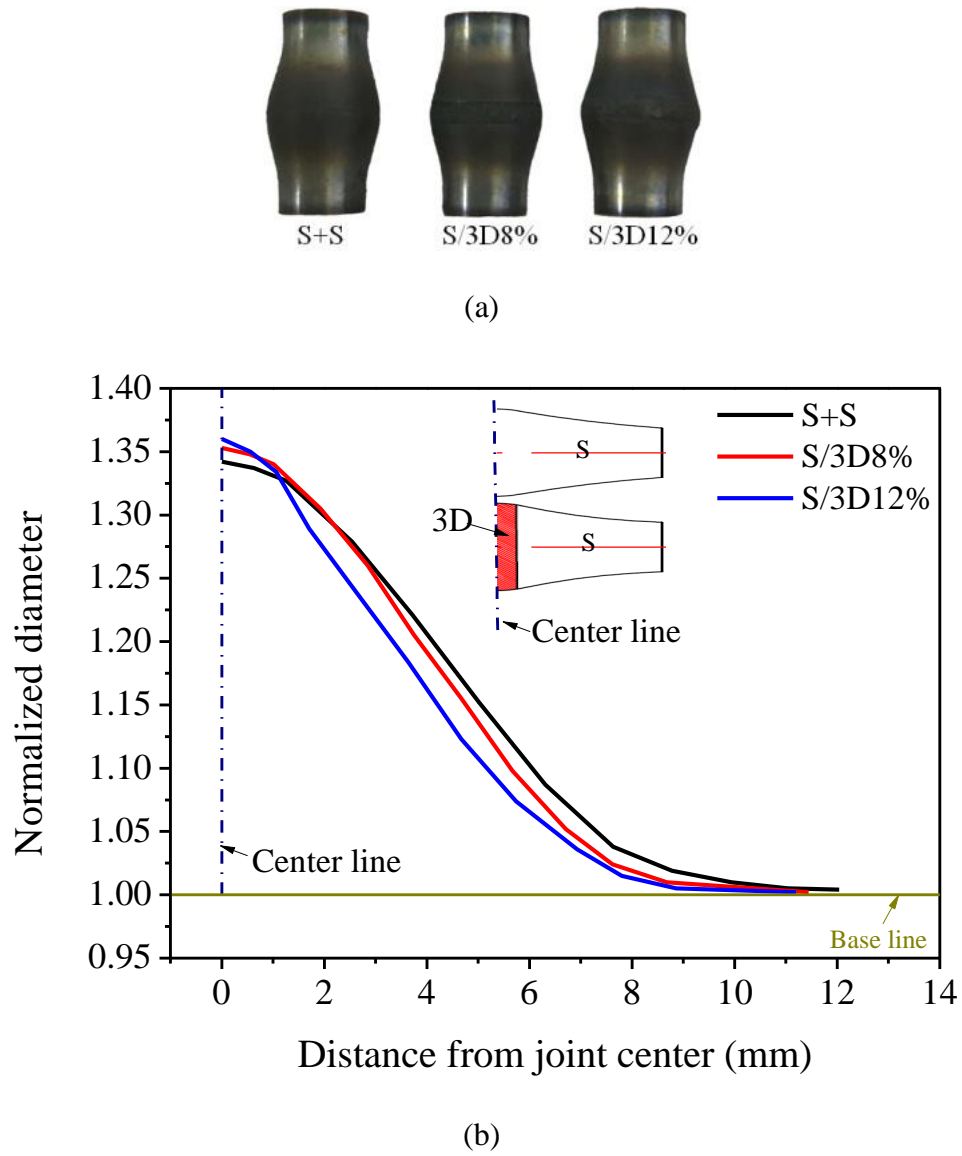
(a)

(b)

Figure 3.6 (a) The appearance of the EAPJ joints with or without the porous interlayer and

(b) normalized diameter profile of the EAPJ joints along the height

However, the existence of the porous interlayer clearly affects the joining load during EAPJ. The load-displacement curve during EAPJ can be divided into three different stages (Figure 3.7(a)). In the first stage (stage I), the joining load initially increases rapidly until the temperature of the specimen assembly (measured in the middle of the assembly) reaches approximately 700~900 ℃, as shown in the temperature history in Figure 3.7(b). Once the joining load reaches the maximum value, the load drastically decreases due to severe softening of the specimen assembly due to resistance heating (stage II). Finally, for the remaining part of the joining process (stage III), the load history nearly shows a plateau at the drastically decreased value, as the elevated temperature was maintained by a pulsed electric current, as shown in Figure 3.7(b). The load-displacement curves during EAPJ shown in Figure 3.7(a) clearly demonstrate that the compressive joining load decreased by using the porous interlayer. Also, the decease of the joining load is more pronounced at the higher porosity of 12 vol.%. The maximum joining loads of the S/3D8% and S/3D12% joints decreased to approximately 85 and 72% of the maximum joining load of the S+S joint, respectively.

The decease of the joining load with the porous interlayer is a result of the combined effects of the lower yield (and flow) stress of the porous interlayer (Figure 3.5) and the higher temperature during joining (Figure 3.7(b)). The higher temperature during joining with the porous interlayer can be simply explained by two reasons. First, the bulk resistivity of the porous interlayer is higher than that of the solid specimen due to the porosity (Ibrahim *et al.,* 2016). The result of the separately conducted measurement of the bulk resistivity confirms the higher bulk resistivity of the porous interlayer (solid: 7.50E-07 $\Omega \cdot m$, 8 vol.%: 11.1E-07 $\Omega \cdot m$, 12 vol.%: 15.4E-07 $\Omega \cdot m$). Secondly, the specimen assembly with the porous

interlayer has two interfaces between the relatively rough surface of the interlayer and the smooth surfaces of the solid specimen, while the specimen assembly without the porous interlayer has only one interface between the smooth surfaces of the solid specimen. Therefore, the resultant electrical resistance of the specimen assembly increases with the existence of the porous interlayer, even though the geometry of the specimen assembly is nearly identical for all cases with or without the porous interlayer. It is also worth noting that drastic softening occurred earlier in the specimen assemblies with the porous interlayer as the temperature increased more rapidly due to the higher electric resistance (Figure 3.7).

The moment temperature profile of S+S joint and S/3D12% joint in the first 5 seconds of continuous electric current application along the height of the specimen assembly during joining clearly shows that the porous interlayer with a relatively higher electric resistance provides rapid and local heating in the specimen assembly, as shown in Figure 3.8.
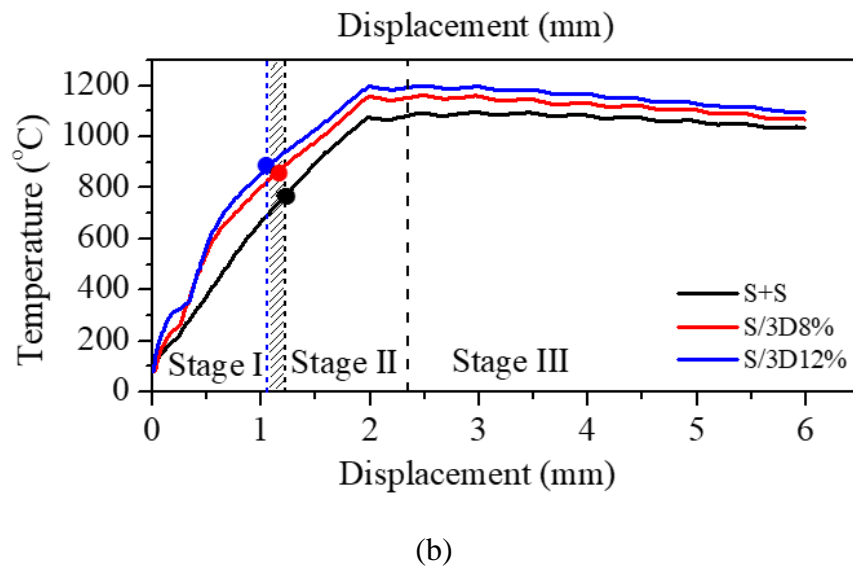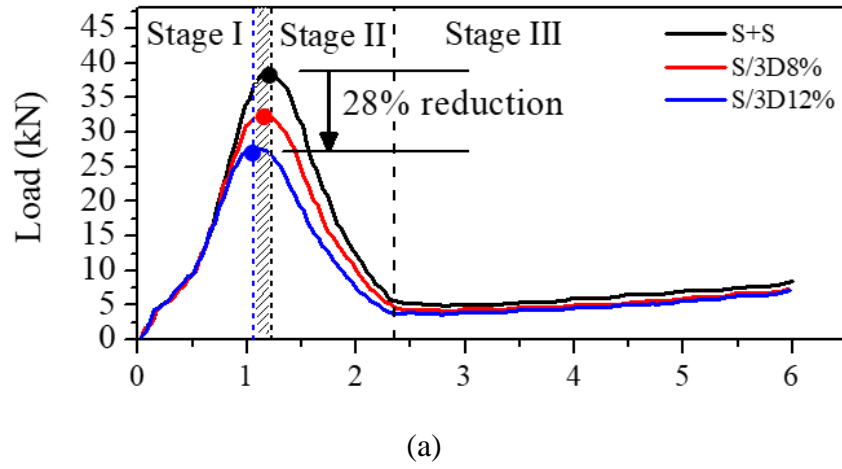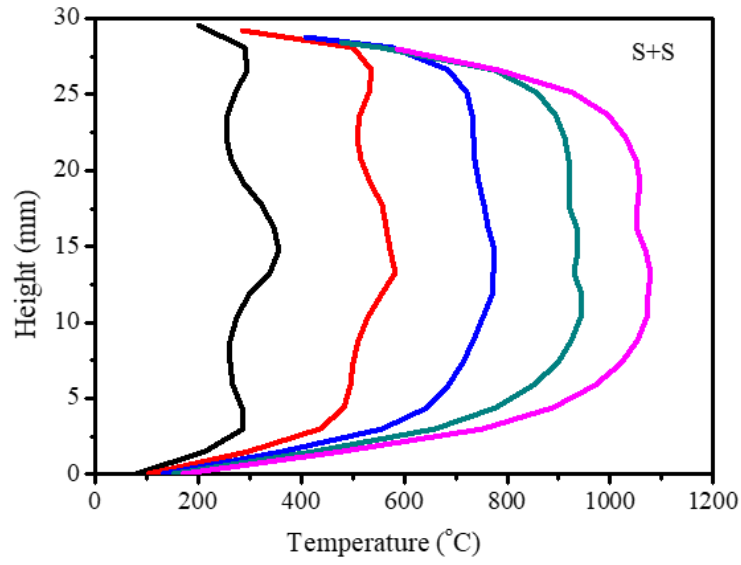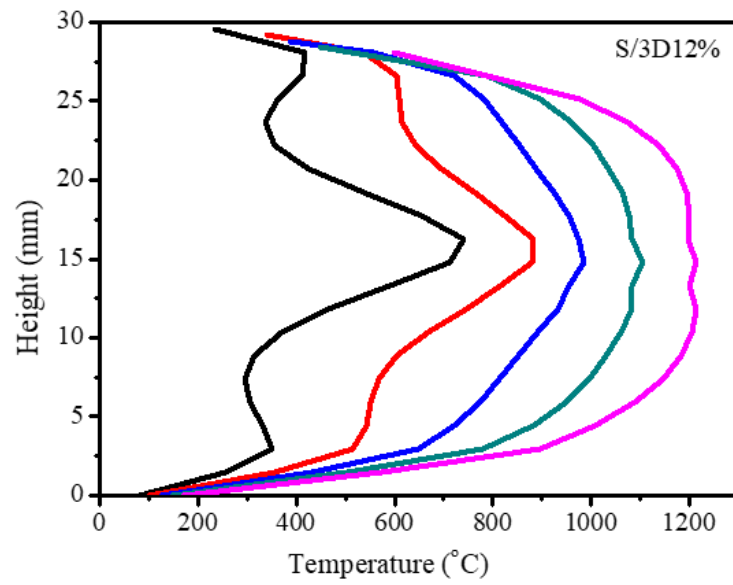
Figure 3.7 (a) Load-displacement curves and (b) maximum temperature histories during

the joining experiments.

(a)

(b)

Figure 3.8 The moment temperature profiles of (a) S+S joint and (b) S/3D12% joint.

The effect of the porous interlayer on the joining load in the present study may be roughly described using the Gibson-Ashby model (Gibson *et al.,* 1997), since the bulk geometry of the porous interlayer is identical for the two different porosities and the geometry of the specimen assembly is also identical for all cases. Based on the maximum joining load, the relative joining load or the relative joining pressure can be written as a function of the relative density as,

$$\frac{P_p}{P_s} = 1.14 \left(\frac{\rho_p}{\rho_s}\right)^{3.52} \tag{3.2}$$

where *P* represents the joining pressure, which is calculated by dividing the joining load by the original cross-sectional area of the specimen assembly perpendicular to the direction of compression. The proportional constant and exponent in the above equation are somewhat different from those obtained for the baseline tests in Eqn. (3.1). This difference is a result of the effect of different elevated joining temperatures and the effect of the relative thickness of the porous interlayer in the specimen assembly.

The optical microscopy (OM) observation of the cross sections along the height of the joint suggests that sound solid-state joints were produced by EAPJ. No macroscopic defects were observed by OM at the joint interfaces for any of the EAPJ joints with or without the porous interlayer (Figure 3.9). For the joint without the porous interlayer (the S+S joint), the interface was hardly recognizable, even after etching, as shown in Figure 3.9(a). For the joints with the porous interlayer (the S/3D8% and S/3D12% joints), the etching revealed interfaces between the porous interlayer and solid specimens due to the slightly different chemical compositions of the solid and powder SUS316L. For example, see Figure 3.9(b). OM also suggests that the porosity in the interlayer was completely eliminated by EAPJ for both the S/3D8% and S/3D12% joints.

69
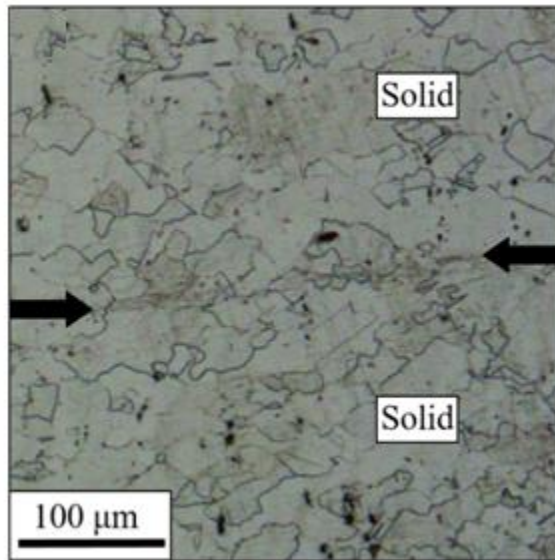
(a)
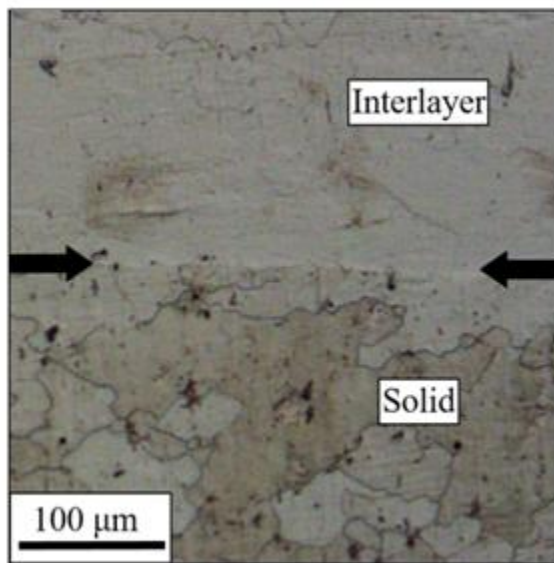
(b)

Figure 3.9 OM at the joint interfaces for (a) S+S and (b) S/3D12% joints. The black arrows approximately mark the joint interfaces.

The inverse pole figure (IPF) map of the cross section along the joining direction of the solid specimen before EAPJ shows nearly equiaxial and homogeneously distributed grains (average grain size of 51.1 μm), as shown in Figure 3.10(a). Also, the IPF map suggests that a large fraction of annealing twins with different orientations exists in the solid specimen before EAPJ. For the 12 vol.% additive manufactured porous interlayer, the IPF map of the cross section along the building direction (same as the joining direction) of the interlayer (Figure 3.10(b)) shows a microstructure consisting of long needle shaped grains along the building direction, which is a result of rapid solidification due to the high cooling rate encountered in the laser sintering process (Ibrahim *et al.,* 2016). The black regions in the IPF map in Figure 3.10(b) correspond to pores. The 8 vol.% porous interlayer shows a quite similar microstructure.
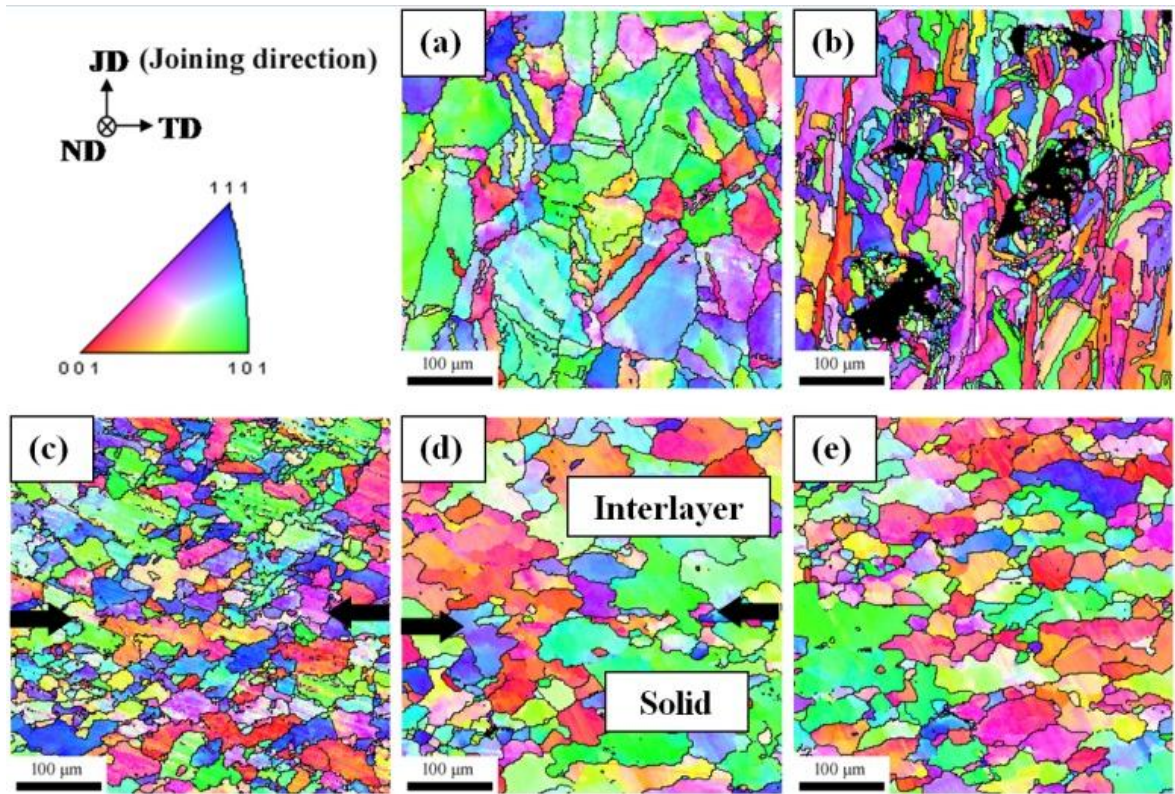
Figure 3.10 IPF maps (ND) of (a) base solid metal, (b) base 12 vol.% porous metal, (c) interface region of S+S joint, (d) interface region of S/3D12% joint and (e) interlayer center region of S/3D12% joint. The black arrows approximately mark the joint interfaces.

The IPF map of the cross section along the height at the joint interface of the S+S joint (Figure 3.10(c)) shows finer grains (average grain size of 29 μm) compared to the solid specimen before EAPJ. Note that no discontinuity of the microstructure was visible across the joint interface, which is approximately marked by the black arrows in Figure 3.10(c). The IPF map of the S+S joint confirms that a sound solid-state joint was produced by atomic diffusion and dynamic recrystallization during EAPJ (Kim *et al.,* 2014; Kim *et al.,* 2017). The IPF maps of the cross section along the height at the joint interface (Figure 3.10(d)) and at the center of the porous interlayer (Figure 3.10(e)) of the S/3D12% joint also confirm that no discontinuity of the microstructure was visible across the joint interface (approximately marked by black arrows) and the porosity in the interlayer was completely eliminated, respectively. In addition, a comparison of the average grain size of the S+S joint interface (29 μm) with that of the S/3D12% joint interface (60.4 μm) suggests that additional grain growth occurred after dynamic recrystallization during EAPJ with the porous interlayer, which is very likely to be due to higher heat input, as shown in Figure 3.7(b). Grain growth in the interlayer during EAPJ was also observed, as revealed in the comparison of Figures 3.10(b) and (e). A similar result was obtained for the S/3D8% joint.

The result of the EDS line scan across the interface (marked by a micro indentation) of the S/3D12% joint shows that the distribution of the major alloying elements (Mo, Ni, Fe, Cr) in the interface and the interlayer is nearly identical to that in the solid specimen, as shown in Figure 3.11. Once again, a quite similar result was obtained for the S/3D8% joint. The SEM micrograph in Figure 3.11(a) and the results of the EDS line scan in Figure 3.11(b) suggest complete densification of the porous interlayer material and achievement of good coalescence between the interfaces in EAPJ with the porous interlayer.

73

(a)

Molybdenum La1, Nickel Ka1, Iron Ka1, Chromium Ka1
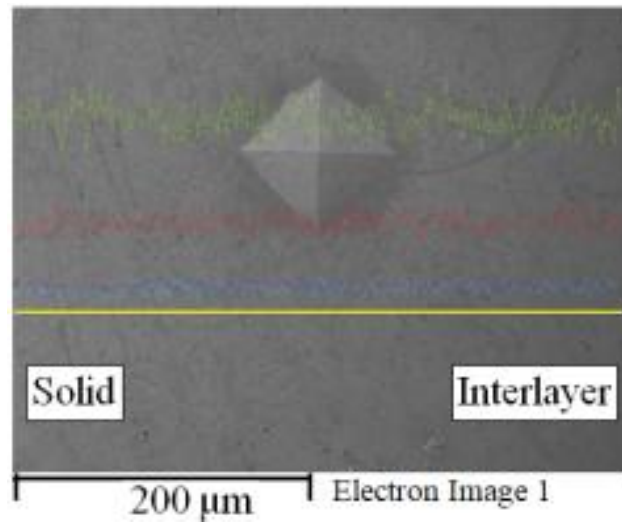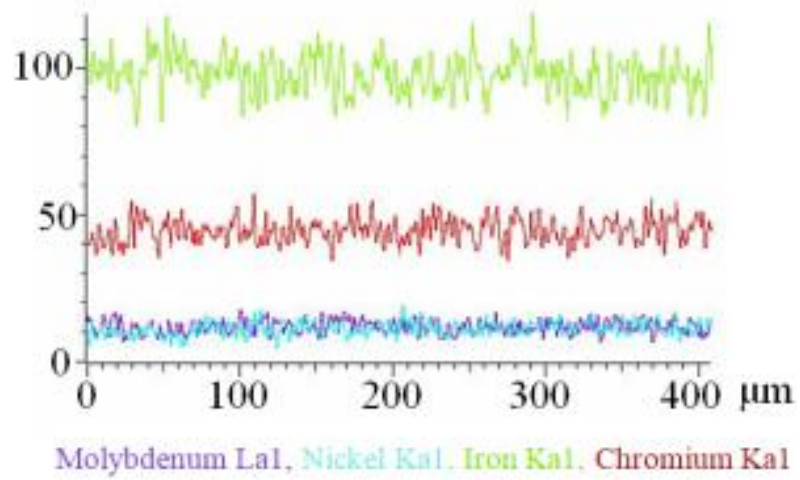
(b)

Figure 3.11 (a) SEM micrograph and (b) elemental line scan analysis of the S/3D12% joint.

The results of the microhardness measurements demonstrate that the hardness distributions are quite uniform and similar for all the EAPJ joints with or without the porous interlayer, especially near the joint interfaces (Figure 3.12).
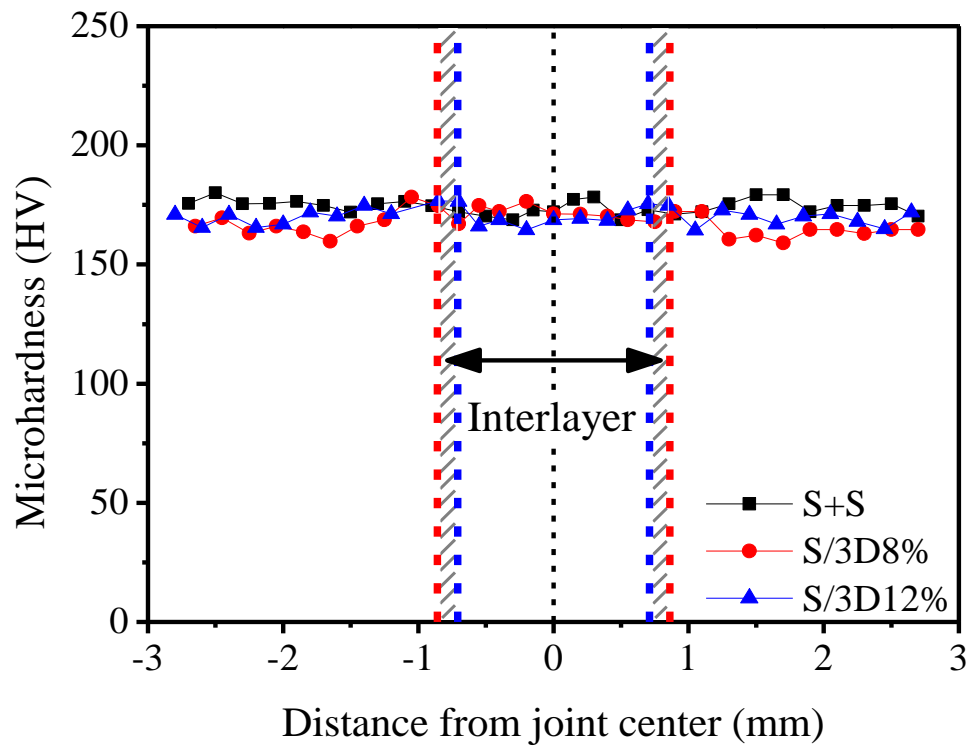
Figure 3.12 Microhardness profile across the joint interface.

The slightly different hardness distributions in the solid regions outside the interlayer should be contributed to the fact that the solid regions experienced different loading conditions depending on the properties of the interlayer. A slightly higher level of grain growth in the solid region of the S/3D8% joint was observed in comparison with the S/3D12% joint probably due to the higher joining load, as shown in Figure 3.13. As a result, the hardness in the solid region of the S/3D8% joint are lower than those of the S/3D12% joint (Figure 3.12). However, the difference is quite insignificant. The microhardness distributions suggest that the mechanical properties of the additive manufactured interlayer became similar to those of the solid regions due to the elimination of porosity and microstructural changes (recrystallization and following grain growth) during EAPJ.
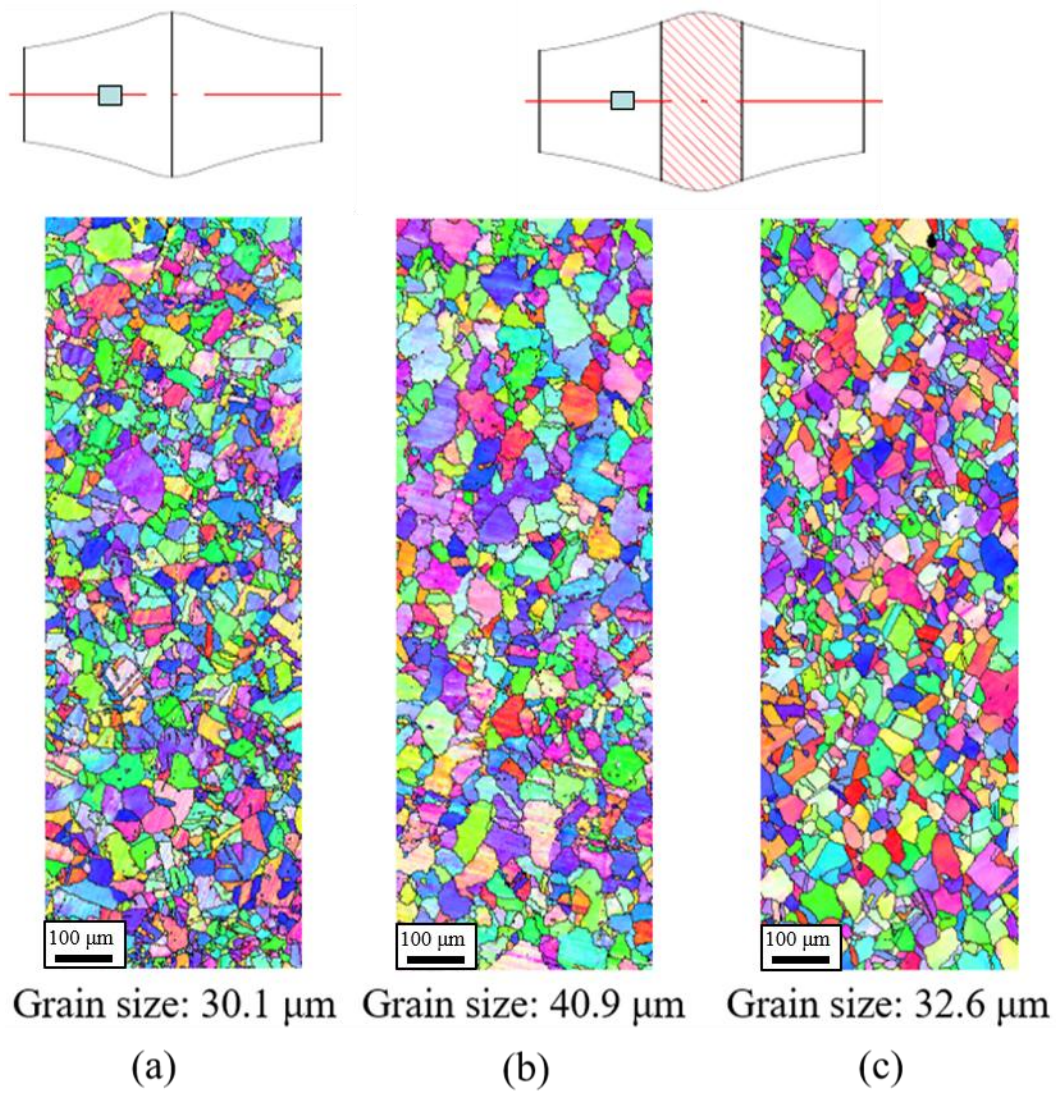
Figure 3.13 The IPF maps of the solid regions (approximately 1 mm away from the interface) of EAPJ joints (a) S+S, (b) S/3D8% and (c) S/3D12%.

For the cantilever bend tests, the joint specimens were machined to a cylinder with a diameter of 8 mm and fixed in a custom-made fixture, as described in Figure 3.14(a). The joint specimen was then bent using a flat punch with a distance from the fixed end to the edge of the punch of 8 mm, as shown in Figure 3.14(a).
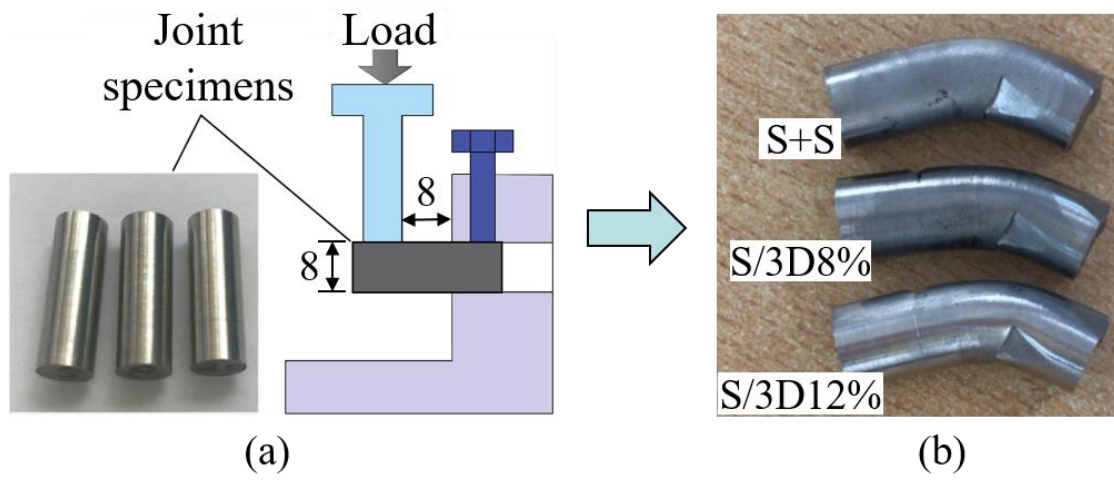
Figure 3.14 (a) A schematic of cantilever test and (b) the result.

Finally, all EAPJ joints with or without the porous interlayer were successfully bent to the maximum deflection until the slippage of the flat punch from the specimen, without fracture (Figure 3.14(b)). This result supports the result in Figure 3.12 that compatible mechanical properties were induced for all the joint configurations considered in the present study.

3.4 Conclusion

Effectiveness of using an additive manufactured metal porous interlayer during EAPJ of bulk specimens was demonstrated. By using the porous interlayer with a lower compressive strength and higher electric resistivity, defect-free joints were successfully fabricated with a lower joining pressure. As confirmed by the microstructural analysis, the porosity in the interlayer was eliminated by the compressive deformation and recrystallization during joining. In fact, the occurrence of grain growth in the joints with the interlayer suggests that the process effectiveness can be further enhanced by adjusting the temperature profiles during EAPJ. The results of the microhardness measurement and cantilever bend test showed that the mechanical properties of the joints with the interlayer are comparable to those of the joint without the interlayer. The result of the present study can be expanded to solid-state joining of dissimilar (or even difficult to weld) bulk components by properly adjusting the structure and chemical composition of the porous interlayer (Hong *et al.,* 2017).

ACKNOWLEDGEMENTS

References

Dewidar MM, Khalil KA, Lim JK (2007) Processing and Mechanical Properties of Porous 316L Stainless Steel for Biomedical Applications. Trans. Nonferrous Met. Soc. China 17:468-473.

Esen Z, Bor S (2007) Processing of Titanium Foams Using Magnesium Spacer Particles. Scripta Materialia 56:341-344.

Gibson LJ, Ashby MF (1997) Cellular Solids: Structure and Properties, 2nd Ed. Cambridge University Press, Cambridge.

Harada Y, Sada Y, Kumai S (2016) Joining Steel Studs and Steel Plates by Solid-state Stud Welding and Estimation of Temperature Near the Joint Interface. Journal of Manufacturing Processes 23(2016)75-82.

Hong ST, Chun DM, Park HS, Han HN, Park JW, Li YF, Nguyen DS (2017) Electrically Assisted Pressure Joining Apparatus and Method. KR Papent No. 10-1921053.

Hong ST, Park HS, Han HN, Jeong HJ, Mondal M, Das H (2017) Method for Locally Reinforcing A Metal Material. KR Papent No. 10-2017-0079197.

Ibrahim KA, Wu B, Brandon NP (2016) Electrical Conductivity and Porosity in Stainless Steel 316L Scaffolds for Electrochemical Devices Fabricated Using Selective Laser Sintering. Materials and Design, 106:51-59.

Kim MJ, Lee KH, Oh KH, Choi IS, Yu HH, Hong ST, Han HN (2014) Electric current-induced annealing during uniaxial tension of aluminum alloy. Scripta Materialia 75:58-61.

Kim MJ, Lee MG, Hariharan K, Hong ST, Choi IS, Kim D, Oh KH, Han HN (2017) Electric current-assisted deformation behavior of Al-Mg-Si alloy under uniaxial tension. International Journal of Plasticity 94:148-170.

Kimura M, Suzuki K, Kusaka M, Kaizu K (2017) Effect of Friction Welding Condition on Joining Phenomena and Mechanical Properties of Friction Welded Joint between 6063 Aluminium Alloy and AISI 304 Stainless Steel. Journal of Manufacturing Processes 26:178-187.

Louw JA, Ghiselin RE (1974) Flash Removal Apparatus for A Friction Welding Operation. US Patent No.3853258.

Mahabunphachai S, Koç M, Ni J (2009) Pressure Welding of Thin Sheet Metals: Experimental Investigations and Analytical Modeling. Journal of Manufacturing Science and Engineering 131(4):041003.

Meshram MP, Kodli BK, Dey SR (2014) Mechanical Properties and Microstructural Characterization of Friction Stir Welded AISI 316 Austenitic Stainless Steel. Procedia Materials Science 5(2014):2376-2381.

Monamed HA, Washburn J (1975) Mechanism of Solid State Pressure Welding. Welding Research Supplement :302-310.

Mori K, Bay N, Fratini L, Micari F, Tekkaya AE (2013) Joining by plastic deformation. CIRP Annals-Manufacturing Technology 62(2):673-694.

Ng MK, Li L, Fan Z, Gao RX, Smith III EF, Ehmann KF, Cao J (2015) Joining Sheet Metals by Electrically-Assisted Roll Bonding. CIRP Annals–Manufacturing Technology 64(1):273-276.

Ozel K, Sahin M, Akdogan A. (2008) Mechanical and Metallurgical Properties of Aluminium and Copper Sheets Joined by Cold Pressure Welding. Journal of Mechanical Engineering 54(11):796-806.

Peng L, Xu Z, Lai X (2014) An Investigation of Electrical-Assisted Solid-State Welding/Bonding Process for Thin Metallic Sheets: Experiments and Modeling. Proceedings of the Institution of Mechanical Engineers, Part B: Journal of Engineering Manufacture 228(4): 582-594.

Roh JH, Seo JJ, Hong ST, Kim MJ, Han HN, Roth JT (2014) The Mechanical Behavior of 5052-H32 Aluminum Alloys Under A Pulsed Electric Current. International Journal of Plasticity 58:84-99.

Sahin M, Misirli C (2012) Properties of Cold Pressure Welded Aluminium and Copper Sheets. Advanced Materials Research, 463-464: 244-248.

Sarsilmaza F, Kirik I, Bati S (2017) Microstructure and Mechanical Properties of Armor 500/AISI2205 Steel Joint by Friction Welding. Journal of Manufacturing Processes 28:131-136.

Xu Z, Peng L, Yi P, Lai X (2013) Study on a novel electrical-assisted pressure welding process of thin metallic foils. Applied Mechanics and Materials 271-272:147-151.

Zheng Q, Feng X, Shen Y, Huang G, Zhao P (2016) Dissimilar Friction Stir Welding of 6061 Al to 316 Stainless Steel Using Zn as A Filler Metal. Journal of Alloys and Compounds 686(2016):693-701.

Zhang W, Bay N (1997) Cold Welding-Theoretical Modeling of The Weld Formation. Welding Research Supplement :417–430.

CHAPTER Ⅳ

SOLID-STATE DISSIMILAR JOINING OF STAINLESS STEEL 316L AND INCONEL 718 ALLOYS BY ELECTRICALLY ASSISTED PRESSURE JOINING

ABSTRACT

Electrically assisted solid-state joining (or electrically assisted pressure joining, EAPJ) of dissimilar stainless steel 316L (SUS316L) and Inconel 718 (IN718) alloys is experimentally investigated. The specimen assembly for the experiment is comprised of two cylindrical solid specimens (SUS316L and IN718) with an identical geometry. In EAPJ, electric current and plastic compression are directly and simultaneously applied to the specimen assembly. The microstructural analysis confirms that crack/void-free joints are successfully fabricated by EAPJ in the selected dissimilar metal alloys without melting and solidification. An obvious atomic diffusion region at the joint interface is identified. The results of tensile tests show that all the joints fracture from the SUS316L side, which undergoes typical ductile fracture with large plastic deformation. The results of the present study confirm that the concept of EAPJ is applicable to solid state joining of dissimilar material combination.

Keywords: Solid-state joining, Dissimilar materials, Stainless steel 316L, Inconel 718, Electrically assisted pressure joining

4.1 Introduction

To achieve better structural performance and higher economic efficiency, combining various materials with different properties into a multi-material hybrid structure is becoming more popular (Martinsen *et al.,* 2015). Stainless steel 316L alloy (SUS316L) is widely used as an engineering material due to its high strength and good corrosion resistance (Kumara *et al.,* 2018). Inconel 718 alloy (IN718) is a precipitation hardened nickel-based super alloy that is used extensively for high temperature applications such as gas turbines, nuclear reactors, and rocket engines due to its ability to maintain high strength, toughness, and good corrosion resistance at elevated temperatures (Tharappel *et al.,* 2018; Ramkumar *et al.,* 2014; Ramkumar *et al.,* 2017). The dissimilar joints of SUS316L and IN718 with their respective advantages have a wide range of applications, for example, the fabrication of high temperature components in aerospace industries and nuclear power plants (Ramkumar *et al.,* 2014; Ramkumar *et al.,* 2017). Henderson *et al.* (2004) reported the use of SUS316L and IN718 bimetallic joints in industrial gas turbine engines. Locci *et al.* (2009) reported that the dissimilar joints of SUS316L and IN718 can be used in the hot-side heat exchanger as a key component of a power conversion system. Ferretti *et al.* (2006) reported that the bimetallic joints of SUS316L and IN718 can be used in the components for international space station.

The joining processes of similar or dissimilar metal alloys can be broadly classified into two major groups: fusion joining and solid-state joining. Several fusion joining processes for dissimilar joining of SUS316L and IN718 have been reported, such as current gas tungsten arc welding (Ramkumar *et al.,* 2014), tungsten inert gas welding (Ramkumar *et al.,* 2017), and electron beam melting additive manufacturing joining (Hinojos *et al.,* 2014). However, fusion joining is associated with distortion and residual stress generation since it involves

melting and solidification (Choi *et al.,* 2002). Fusion joining of dissimilar metals poses a difficult challenge due to the different melting temperatures and coefficients of thermal expansion. Further, metallurgical issues related to the melting and solidification such as segregation of elements, Laves phase, solidification cracking, and liquation cracking may occur (Cortes *et al.,* 2018; Lin *et al.,* 2014; Iturbe *et al.,* 2016). A proper filler material is required in conventional fusion joining of dissimilar metal alloys (Ramkumar *et al.,* 2014).

As an alternative to fusion joining, solid-state joining is becoming attractive to avoid joint defects caused by melting and solidification in fusion joining. Also, solid-state joining generally does not need filler materials or any fluxes. Examples of solid-state joining include friction stir welding, friction joining, and pressure joining. Except for friction stir welding, which generates a solid-state joint by mechanical stirring of metals using a rotating tool, other solid-state joining processes generally produce joints by establishing diffusion bonding between metal surfaces under pressure. Friction joining, which is frequently used to join bulk parts, can be conducted without external heat due to the presence of frictional heating at the joint interface. However, a complex brake system is necessary during friction joining (Damodaram *et al.,* 2013; Liu *et al.,* 2018; Smith *et al.,* 2016). No additional frictional heat is generated at the final upsetting stage, which actually generates a solid-state joint. Pressure joining can also be used to join similar or dissimilar metal alloys. This joining is generally conducted by plastic deformation at elevated temperatures (Mori *et al.,* 2013). However, in conventional pressure joining, complex heating and control facilities such as programmable furnaces and induction heaters are generally required. Thermal effects on the surrounding parts of the workpieces are also unavoidable due to the non-local heating mode in this process.   In addition, a sufficiently long diffusion time (easily up to a few hours) is

required in conventional pressure joining. For example, Locci et al. (2009) carried out hot pressure joining of SUS316L and IN718 in vacuum for 2 hrs at 1000 K or 1150 K with a pressure of 90 MPa.

To overcome or minimize the drawbacks of friction joining and conventional pressure joining, electrically assisted pressure joining (EAPJ) has been proposed as a new solid-state joining technique (Peng *et al.,* 2014). In EAPJ, electric current is directly applied to the joining specimens under continuous axial deformation. EAPJ possesses several technical advantages over conventional hot pressure joining, such as rapid and local heating, simple and cost-effective process facilities, and much shorter process time (a few seconds) (Hong *et al.,* 2018). When joining bulk workpieces, EAPJ also provides several advantages compared with friction joining. First, EAPJ requires only a simple process set up since the complex rotation and brake systems are avoided. Second, process optimization is relatively easy in EAPJ since the heating of the interface can be continued during the final axial compression. Finally, EAPJ using resistance heating as a heat source may result in the electroplastic effect (Roh *et al.,* 2014; Kim *et al.,* 2014; Kim *et al.,* 2017), which enhances the mobility and diffusion of atoms and improves the mechanical/material properties of joints.

EAPJ is applicable to joining thin metal foils (Peng *et al.,* 2014; Xu *et al.,* 2013; Ng *et al.,* 2015), structural metal sheets (Li *et al.,* 2018), and buck components (Hong *et al.,* 2018; Harada *et al.,* 2016; Hong *et al.,* 2018). Peng *et al.* (2014) successfully applied EAPJ to join brass/brass and steel/steel foils. Xu *et al.* (2013) studied the joining of thin foils of SUS316L by EAPJ. Ng *et al.* (2015) investigated electrically assisted roll bonding of aluminum to aluminum or copper sheets. Li *et al.* (2018) reported that Grade 1 titanium sheets with 1 mm thickness were successfully joined by EAPJ. Harada *et al.* (2016) conducted solid-state

projection joining of steel studs and steel plates using a similar principle to EAPJ. Hong *et al.* (2018) successfully joined SUS316L cylindrical bulk specimens with or without an additive manufactured metal porous interlayer by EAPJ. Unfortunately, studies on the applicability of EAPJ in bulk joining of dissimilar metal alloys are still limited. In the present study, dissimilar joining of SUS316L and IN718 by EAPJ is investigated with microstructural analysis and mechanical testing of the joint.
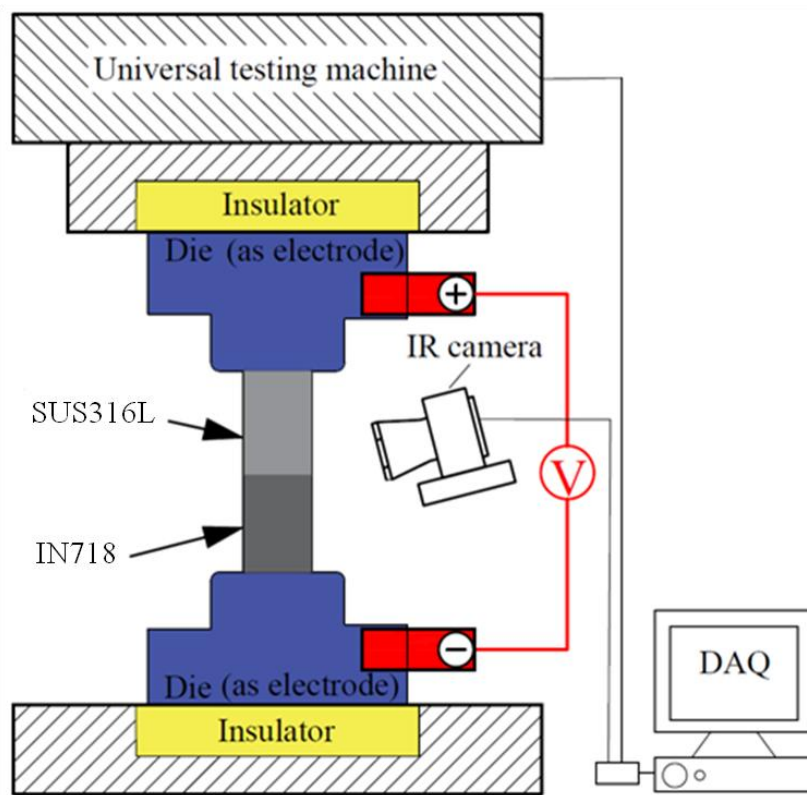
4.2 Experimental set-up

The specimens employed in the present study are cylindrical bulk metals of SUS316L and IN718 with a diameter of 10 mm and a height of 15 mm (Figure 4.1(a)). The chemical compositions of the base metals (BMs) are presented in Table 4.1. Prior to the experiments, the end surfaces of specimens were ground with 320-grit sandpaper to remove the oxide layer, then the specimens were thoroughly cleaned with acetone to remove any grease or dirt.

For EAPJ, a custom made fixture (Hong *et al.,* 2018) was installed in a universal testing machine (DTU900-MH, Daekyoung, South Korea), as described in Figure 4.1(b). The resistance heating was induced during compression for joining by a non-continuous electric current, which was created by a programmable current generator (Vadal SP-1000U, Hyosung, South Korea). Upper and lower dies made of tool steel for compression were also used as electrodes. A set of Bakelite insulators was inserted between the dies and the universal testing machine to isolate the electricity from the testing equipment.
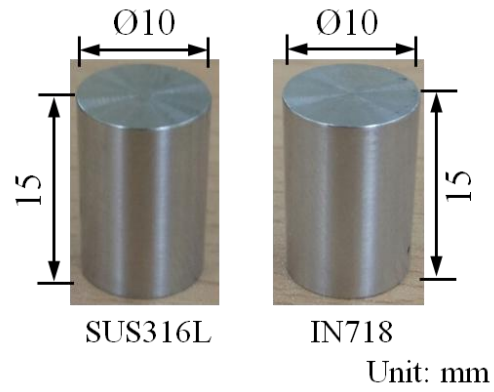
(a)

(b)

Figure 4.1 (a) Cylindrical specimens of SUS316L and IN718 alloys for joining , and (b)

schematic of experimental set-up.

Table 4.1 The nominal chemical compositions of base metals.

(alloying elements, wt%)

	Fe	C	Mn	Si	Cr	Mo	Ni
SUS316L	Rem.	≤0.03	≤2.0	≤0.75	≤18.0	≤3.0	≤14.0
IN718	17	≤0.08	≤0.35	≤0.35	20	3.2	At balance
	Nb	Ti	Cu	Other elements			
SUS316L				P- ≤0.045; S- ≤0.03; N- ≤0.10			
IN718	5.03	0.65	≤0.3	Al-0.2; B-≤0.006; P-≤0.015; S-≤0.015			

During EAPJ, a preload of 100 N was applied to the specimen assembly by the universal testing machine to ensure good contact between the dies (electrodes) and the specimens to avoid sparks between them. Then axial compression and an electric current were simultaneously applied to the specimen assembly, as schematically described in Figure 4.2. A constant displacement rate of 24 mm/min and a maximum displacement of 9 mm were used for all EAPJ experiments.

The electric current parameters for the combination of a continuous electric current and a pulsed electric current in Figure 4.2 are listed in Table 4.2. The initially applied continuous electric current was used to rapidly increase the temperature of the specimens. A pulsed electric current was then applied to the specimen assembly to enhance atomic diffusion at the interface by maintaining the elevated temperature without overheating the specimens. After compressive displacement, the pulsed electric current was continued to maintain the elevated temperature and the electricity for a specified holding time (electric current holding time) at the final compressive displacement to further promote diffusion at the joining interface. Finally, after the completion of electric current holding time, the compressive load was released. In the present study, two different electric current holding times, 0.5 sec and 36.5 sec, were considered. For simplicity, the joints with the two different electric current holding times were identified as H-0s and H-36s, respectively (Figure 4.2 and Table 4.2). To verify the repeatability of the results, the joining experiments were conducted at least three times for each parameter set. The load history during EAPJ was recorded using a PC-based data acquisition system. The temperature of the specimen assembly during joining was also continuously monitored and recorded using an infrared thermal imaging camera (FLIR-T621, FLIR, Sweden).
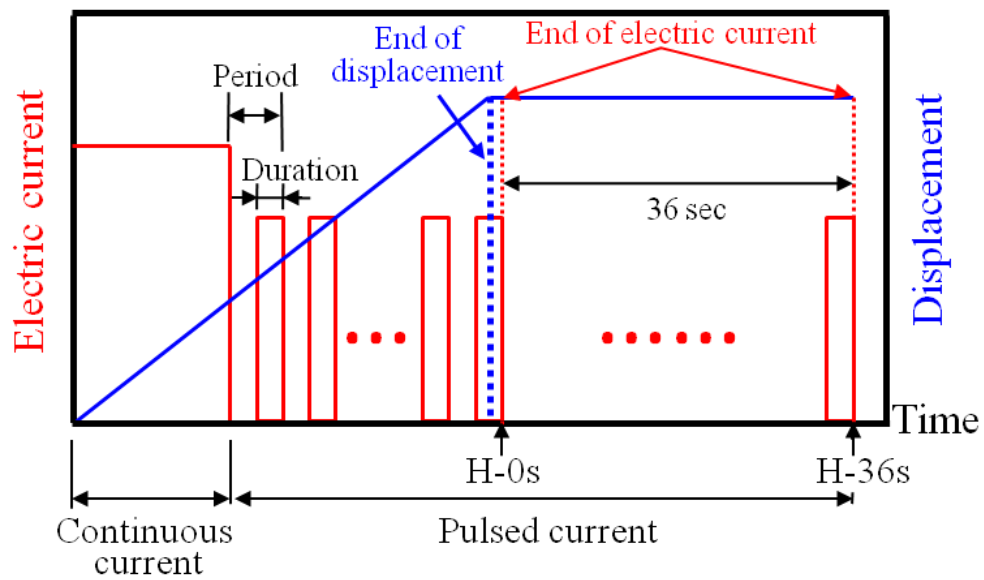
Figure 4.2 Schematic of applying electric current during compressive displacement.

Table 4.2 Electric current parameters of joining experiments.

Step	Nominal current density (A/mm2)	Current duration (sec)	Pulse period (sec)	Total time (sec)
Continuous current	28	5	---	5
Pulsed current	20	1.1	2	H-0s: 18 H-36s: 54

For microstructural analysis, the cross section of the dissimilar joint was prepared along the joining direction. The microstructure of the dissimilar joint was examined using a field emission scanning electron microscope (FE-SEM: SU70, Hitachi, Japan) equipped with an electron backscatter diffraction system (EBSD: EDAX-TSL Hikari, USA) and an energy dispersive spectrometer (EDS: X-Max50, Horiba, Japan). A critical misorientation angle of 15 °was used for grain identification.

The mechanical properties of the dissimilar joint were evaluated by Vickers hardness measurements (2.94 N, 10 sec) on the cross section along the center line in the joining direction using a Vickers indenter (HM-100, Mitutoyo, Japan). Finally, to further confirm sufficient joint strength, uniaxial tensile tests were carried out with a displacement rate of 0.5 mm/min at room temperature. Due to the limited capacity of the electric current generator used in the present study, the size of the joint was not big enough to fabricate a standard tensile specimen. Instead, the dissimilar joint was machined into a dumbbell shape for the tensile test, as described in Figure 4.3(a). A custom-made fixture was designed to fix the machined joint specimen (Figure 4.3(b)).

Ø10

4.5

SUS316L

12

Ø5

4.5

IN718

Unit: mm

(a)

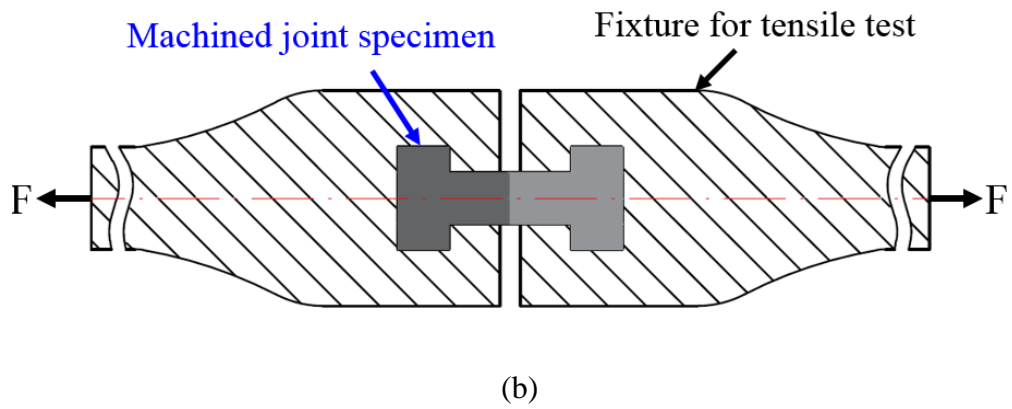Machined joint specimen

Fixture for tensile test

F ← → F

(b)
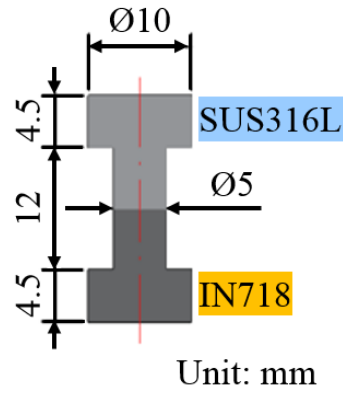
Figure 4.3 Schematics of (a) machined joint specimen and (b) tensile test.

4.3 Results and discussion

No significant difference in appearance was observed among the EAPJ joints with different electric current holding times (Figure 4.4). Obvious and similar flash formation was observed for both EAPJ joints, as shown in Figure 4.4.

The similarity of the load and maximum temperature histories of the H-36s joining to those of the H-0s joining until the end of the displacement confirms the good repeatability of the experiment (Figure 4.5). Three different stages (Hong *et al.,* 2018) were clearly identified in the load history during EAPJ (Figure 4.5(a)). At first, the joining load increased rapidly to the maximum value as the temperature of the specimens increases, as shown in Figure 4.5(b). Then the load drastically decreased after the maximum load due to severe softening of the specimens induced by resistance heating. Finally, the load maintained the decreased value as the elevated temperature was maintained by a pulsed electric current, as shown in Figure 4.5(b). Note that the load increased slightly near the end of displacement (Figure 4.5(a)) due to the decrease in height to diameter ratio of the specimen assembly. Further, the maximum temperature slightly decreased as the displacement increases since the resultant resistance of the specimen assembly decreases with the decrease of the height to diameter ratio (Figure 4.5(b)). After the completion of displacement, the temperature reached a stable value ~ 825 °C under the remaining pulsed electric current.
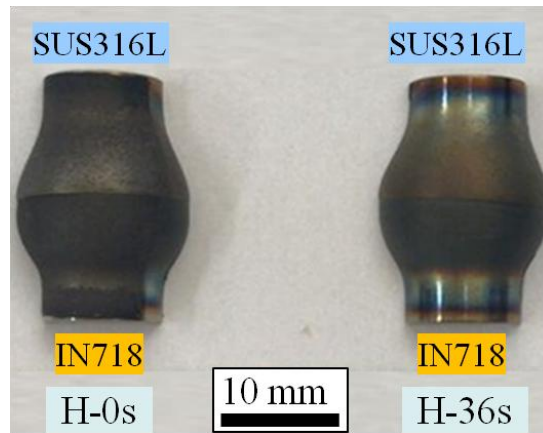
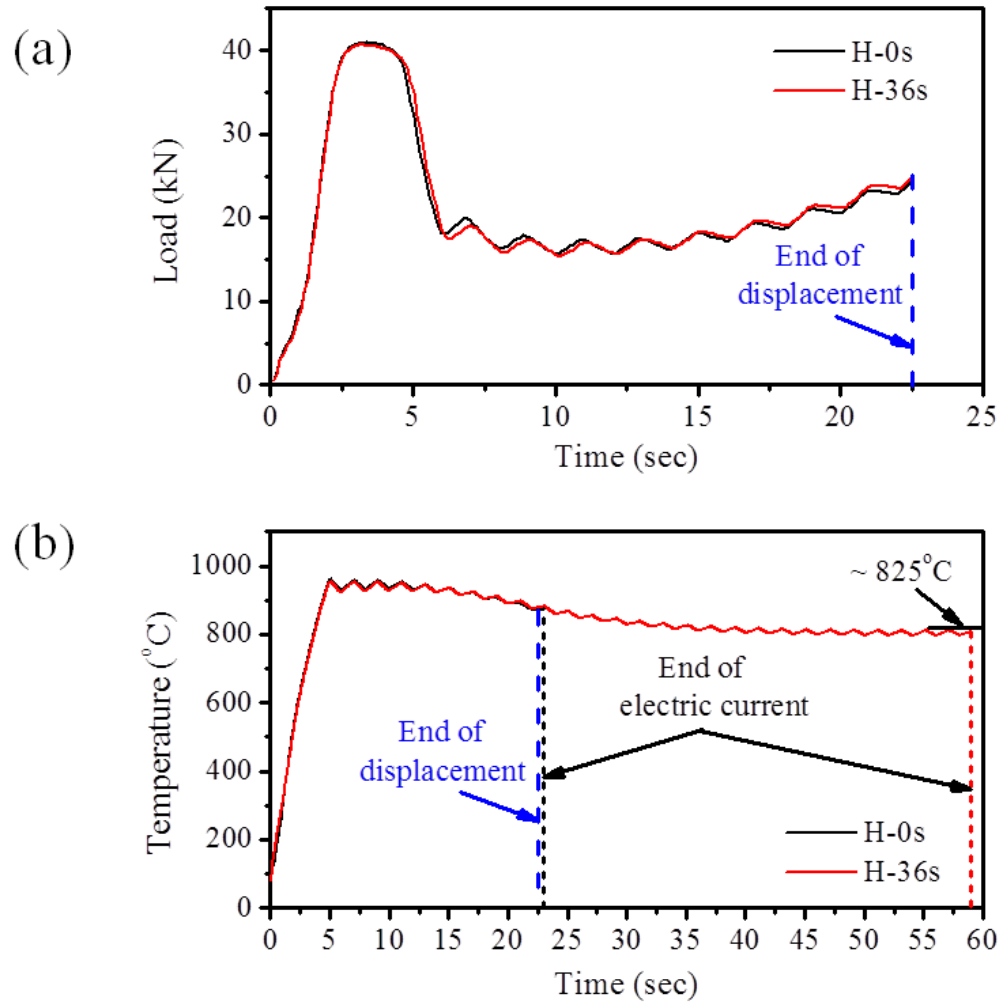Figure 4.4 EAPJ joints of SUS316L and IN718 alloys.

Figure 4.5 Process responses during EAPJ: (a) load and (b) maximum temperature histories.

Temperature profiles of H-0s joint along the joint height at each second in the continuous electric current stage clearly indicate that the temperature raises rapidly to target value by resistance heating (Figure 4.6). Also the temperature of the IN718 side is higher than SUS316L side due to a relatively higher electric resistance.

The OM of the SUS316L BM shows an equiaxed grains structure with a large fraction of annealing twins, as shown in Figure 4.7(a). Compared with the SUS316L BM, much smaller grains were observed in the OM of the IN718 BM. The IN718 BM also exhibits equiaxed and homogeneously distributed grains with a large amount of twins (Figure 4.7(b)).
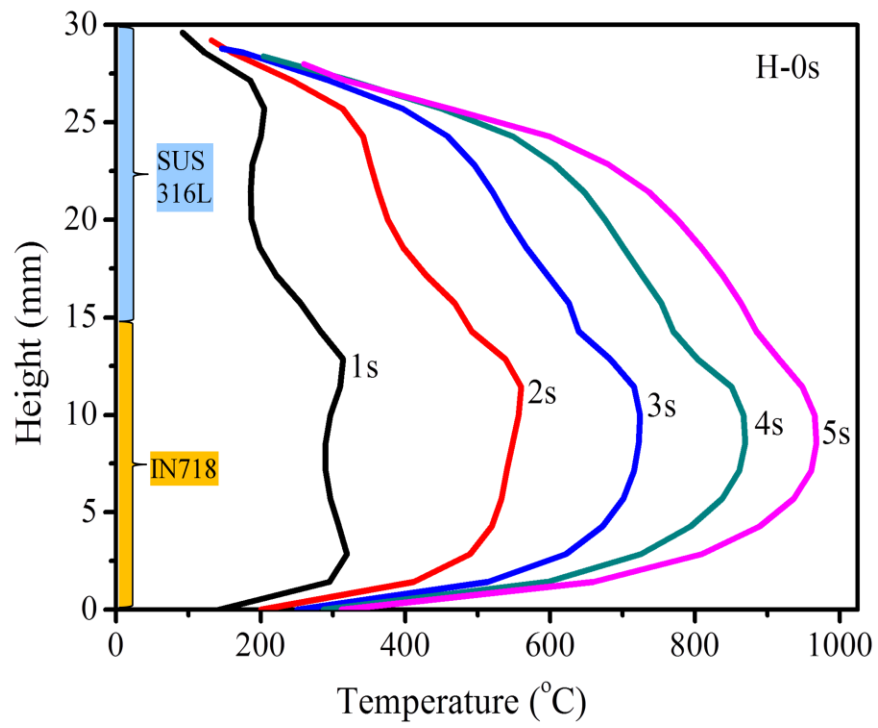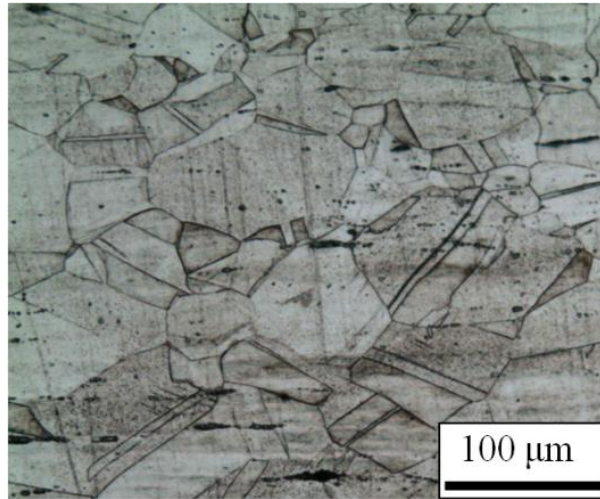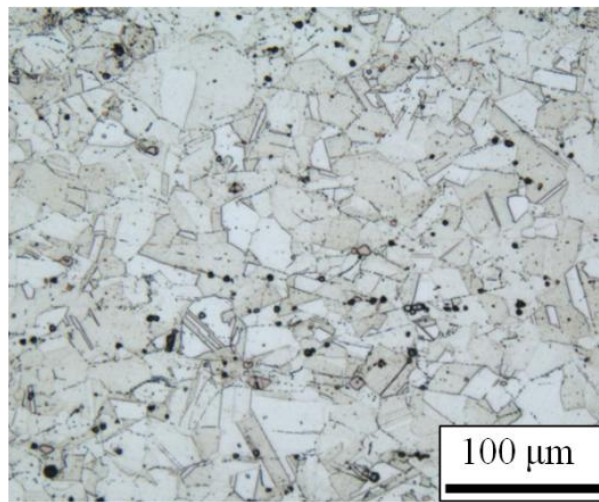
Figure 4.6 Each second moment temperature profile of H-0s joint along the joint height in

the continuous current stage.

(a)

(b)

Figure 4.7. OM images of BMs of (a) SUS316L and (b) IN718.

EBSD inverse pole figure (IPF) maps (normal direction) on the cross section along the height direction (joining direction) for the SUS316L and IN718 BMs are shown in Figures 4.8(a) and (c). Compared with the SUS316L BM, much smaller grains were observed in the IPF maps of the IN718 BM. The IN718 BM also exhibits equiaxed and homogeneously distributed grains with a large amount of twins. The average grain sizes of the SUS316L and IN718 BMs were identified as 64.6 ± 27.9 μm and 32.8 ± 13.2 μm, respectively. The grain orientation spread (GOS) maps with the threshold value of $2°$ for the SUS316L and IN718 BMs identified the fractions of fully annealed or recrystallized grains as 24.5% and 98.0%, respectively (Figures 4.8(b) and (d)).
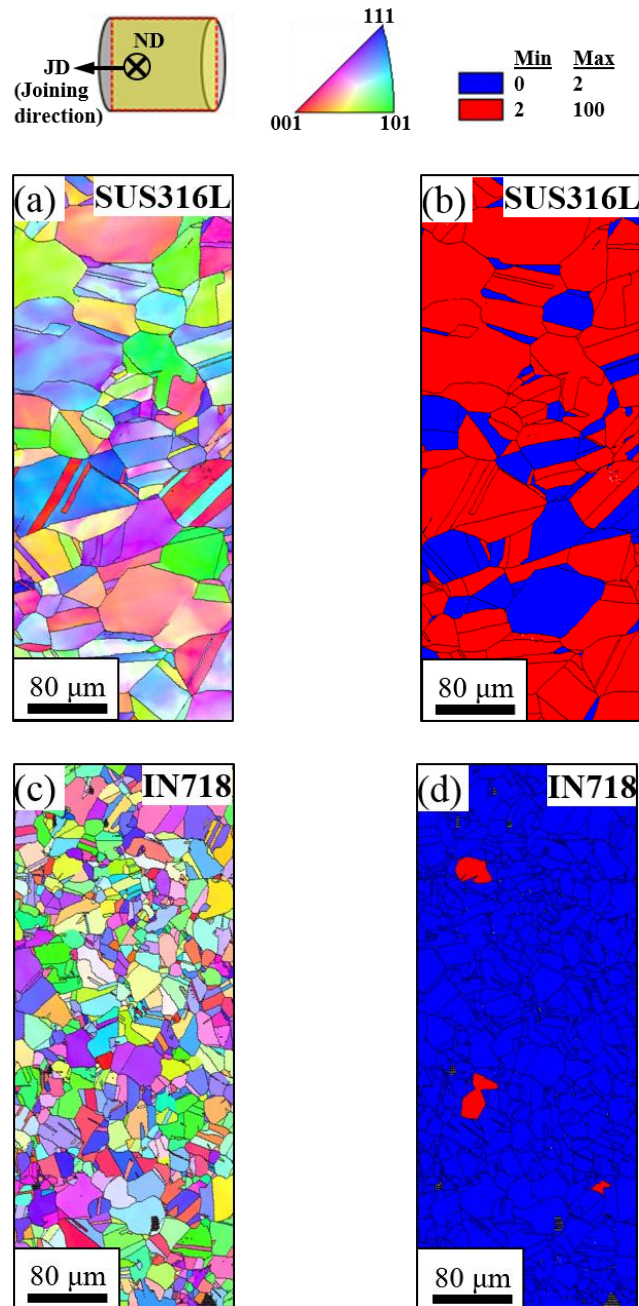
Figure 4.8 (a) IPF (ND) and (b) GOS maps of SUS316L BM; (c) IPF (ND) and (d) GOS

maps of IN718 BM.

The results of SEM on the cross section along the joining direction at the interface of the joints show that sound solid-state joints were produced by EAPJ for both H-0s (Figure 4.9(a)) and H-36s (Figure 4.10(a)) joining. No specific macroscopic or microscopic crack/void was observed at the interface on either joint. The thickness of the diffusion zone can be approximated by the distribution of major alloying elements across the interface through the EDS line scan. The EDS line scan results in Figures 4.9(b)-(c) and 4.10(b)-(c) show that the concentrations of the elements (Fe, Ni, Mo, Nb, and Ti) gradually change within the diffusion zone for the both EAPJ joints. These results indicate that atomic diffusion obviously occurred at the joint interface during EAPJ. The thickness of the diffusion zone of the H-36s joint (approximately 1.9 μm) is significantly larger than that of the H-0s joint (approximately 1.2 μm), as shown in Figures 4.9(b)-(c) and 4.10(b)-(c). The thicker diffusion zone for the H-36s joint can be simply explained by the enhanced atomic diffusion with increased electric current holding time. Additionally, the relatively high concentration of alloying elements of Mo and Nb in the diffusion zone, especially for the H-36s joint, suggests segregation of second phases, such as carbides and Laves phases (Hinojos *et al.,* 2016; Naffakh *et al.,* 2009).
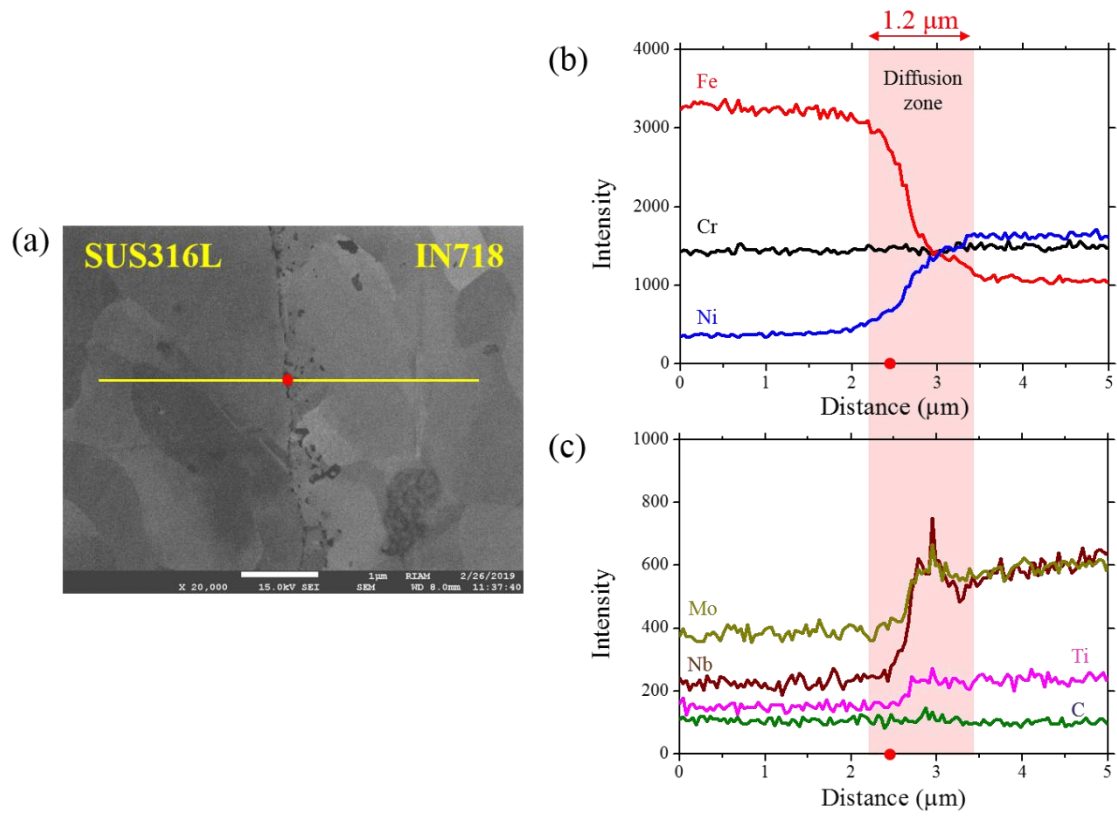
Figure 4.9 (a) SEM micrograph and (b-c) elemental line scan across the joint interface (H-0s).
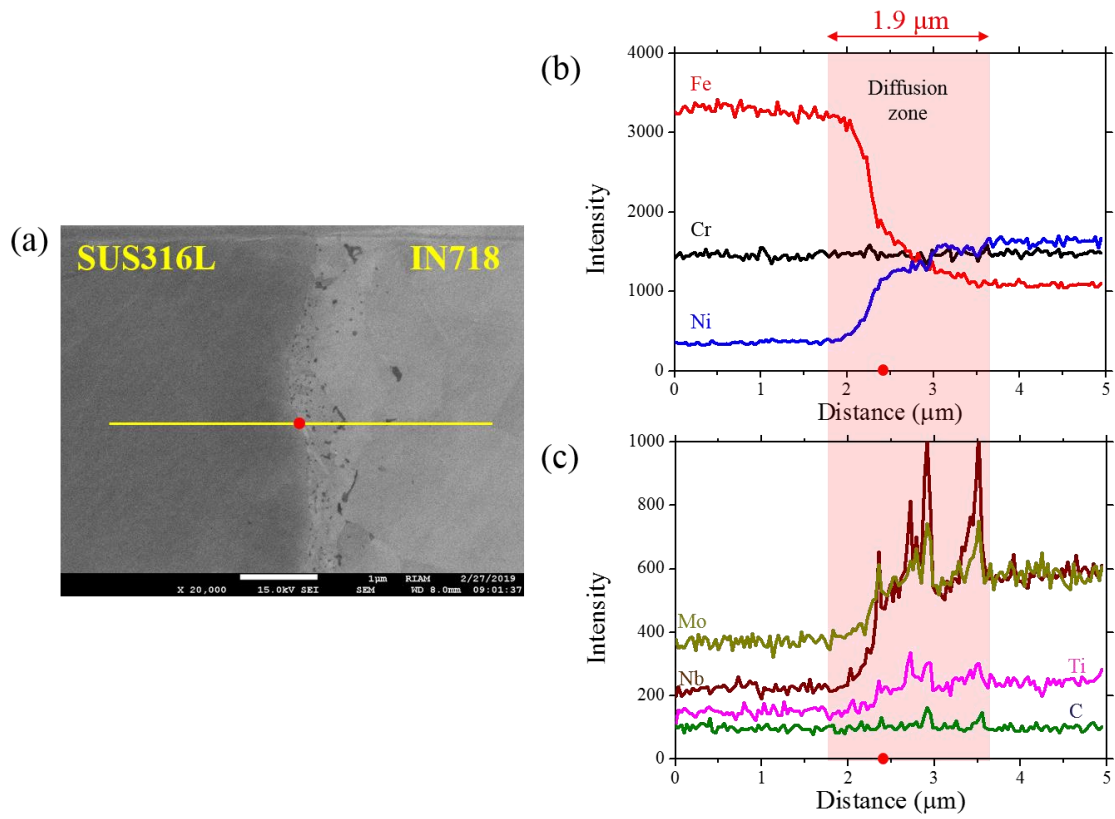
Figure 4.10 (a) SEM micrograph and (b-c) elemental line scan across the joint interface (H-36s).

The IPF and GOS maps on the cross section along the joining direction for the both EAPJ joints are shown in Figure 4.11. For the H-0s joint (Figures 4.11(a) and (c)), both deformed grains and fine equiaxed grains were observed in the SUS316L and IN718 sides. It could be understood that the fine equiaxed grains observed in SUS316L and IN718 sides were generated by recrystallization during EAPJ. As shown in the GOS map of Figure 4.11(c), the fraction of recrystallized region on the IN718 side is much higher than that of the SUS316L side. In the IPF and GOS maps for the H-36s joint (Figures 4.11(b) and (d)), higher numbers of fine equiaxed grains (recrystallized grains) were observed in both SUS316L and IN718 sides compared with the H-0s joint. This suggests that the recrystallization in the H-36s joint was significantly enhanced.

Figure 4.11 IPF maps (ND) of (a) H-0s and (b) H-36s joints; GOS maps of (c) H-0s and (d)
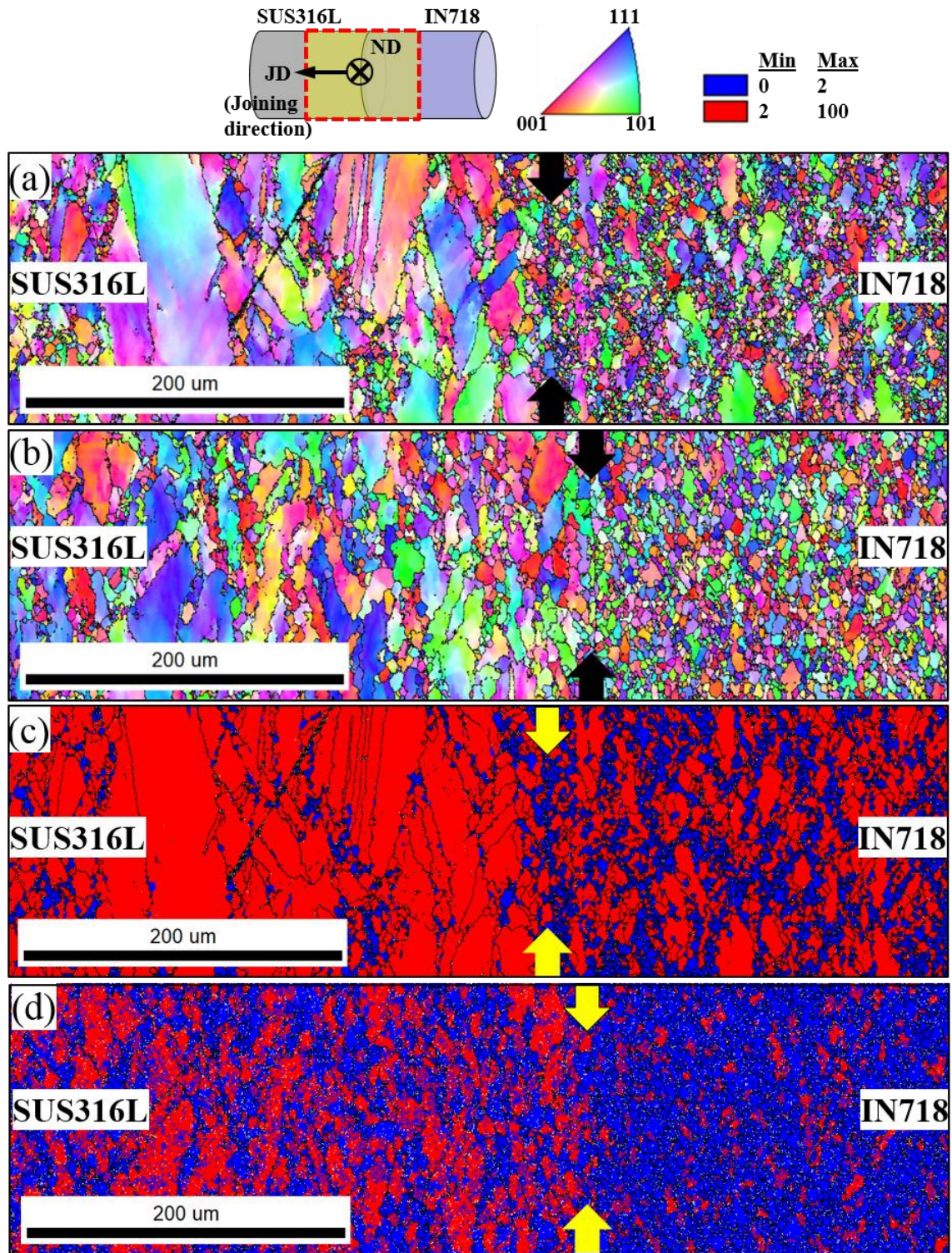
H-36s joints. The black and yellow arrows approximately mark the joint interface.

For both EAPJ joints, the microhardness measurements (Figure 4.12) show that the IN718 side exhibits higher hardness values than the SUS316L side. As a result, the hardness exhibits a steep transition across the interface. Also, note that for both EAPJ joints, the IN718 side of the joint exhibits higher hardness than the BM. For the H-0s joint, the increased hardness of the IN718 side compared with the IN718 BM can be understood as a combined result of strain hardening (red region in the GOS map of Figure 4.11(c)) and grain refinement (7.8±7.1 µm) by recrystallization induced by the elevated temperature and electric current (Kim *et al.*, 2014). In contrast, for the H-36s joint, the increased hardness of the IN718 side in comparison with the IN718 BM seems to be mostly a result of the grain refinement (2.8±1.5 µm) by recrystallization, as shown in the GOS map of Figure 4.11(d). In addition, the hardness of the SUS316L side is lower than that of the SUS316L BM for both EAPJ joints. The decreased hardness can be simply explained by the relatively low fraction (24.5%) of fully annealed or recrystallized grains of the SUS316L BM, as shown in Figure 4.8(b). Due to the pre-existing strain hardening in the SUS316 BM, recrystallization during EAPJ resulted in a lower hardness, even though grain refinement had occurred, especially in the H-36s joint (4.9±4.0 µm). The results of the microhardness measurements correspond well with those of the microstructural analysis.
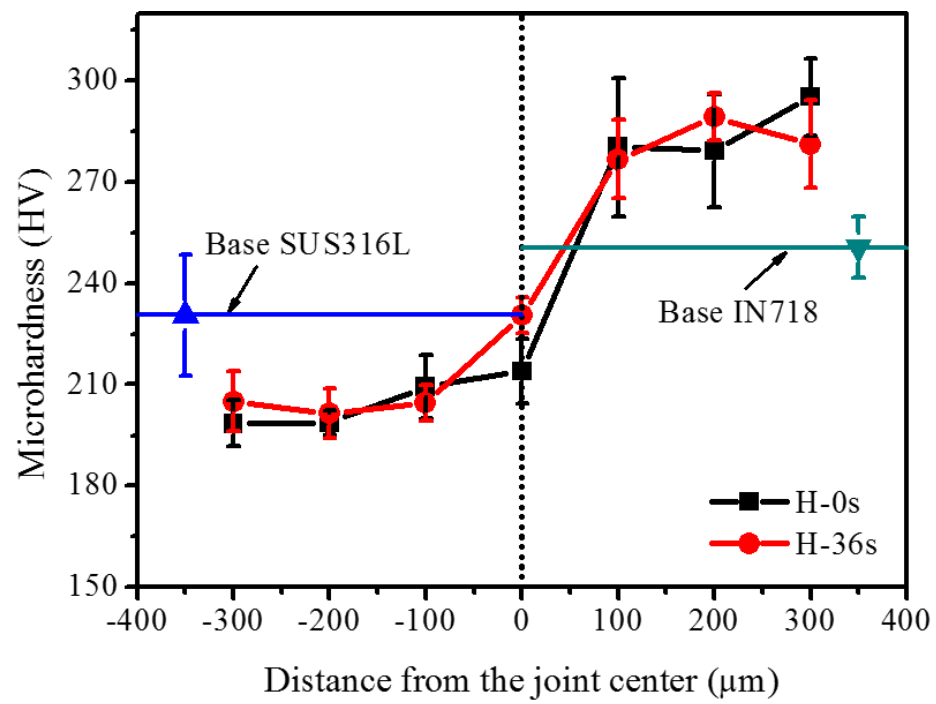
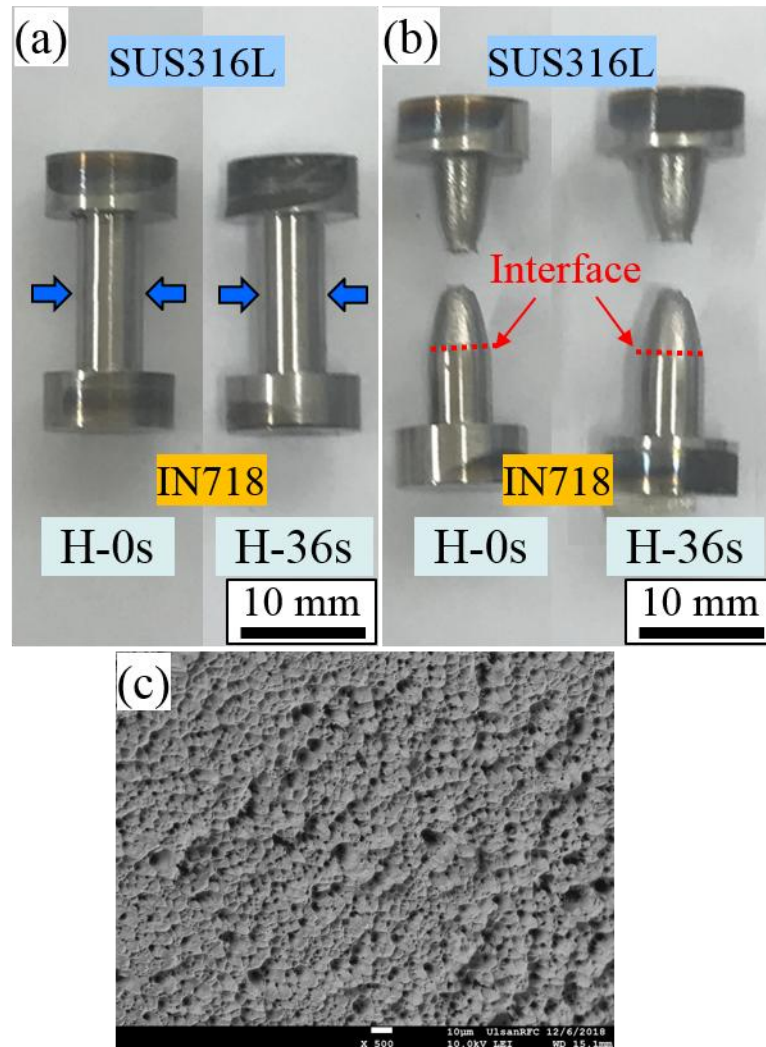Figure 4.12 Microhardness profiles across the joint interface.

Figure 4.13 (a) Machined joint specimens, (b) tensile fractured specimens, and (c) a fracture surface of tensile tested specimen (H-0s).

As shown in Figure 4.13(a), after being machined into a dumbbell shape for tensile tests, the joint interface (approximately marked by blue arrows) was hardly recognizable for the both H-0s and H-36s joints. For the both H-0s and H-36s joints, no interfacial fracture occurred during the tensile tests. Typical ductile fracture with cup and cone formation occurred in the SUS316L side for the both cases, as shown in Figure 4.13(b). The SEM image of the fractured surface with micro-voids and dimples confirms the ductile fracture mode, as shown in Figure 4.13(c) for the H-0s joint. The hardly recognizable interface and the ductile fracture in the SUS316L side confirm the generation of sound joints by EAPJ. Note that almost no deformation was observed in the IN718 side during the tensile test, while the SUS316L side experienced a distinct shape change to ductile fracture, due to the significantly higher mechanical strength of the IN718 side than that of the SUS316L side, as shown in Figure 4.12.

The tensile engineering stress-strain curve of the H-0s joint is similar to that of the H-36s joint, since the deformation and fracture occurred only in the SUS316L side for both cases (a representative result in Figure 4.14). However, the tensile strength of the H-0s joint (691±2.65 MPa) is still slightly higher than that of the H-36s joint (683±3.61 MPa), which reflects the effect of additional electric current holding time for the H-36s joint, as discussed above with the microstructural observation and the hardness measurements. Note that the engineering strain in Figure 4.14 was calculated based on the gage section length of the dumbbell specimen to simplify the analysis. The tensile tests confirmed that a sound and strong solid-state joint can be established with a relatively short process time by EAPJ for the selected dissimilar metal alloys, while the diffusion depth and the concentration of the elements across the interface are affected by the length of electric current holding time. The

effectiveness of the EAPJ can be attributed to the combined effect of elevated temperature by resistance heating, athermal electric current effect (Park *et al.,* 2017), and compressive pressure.
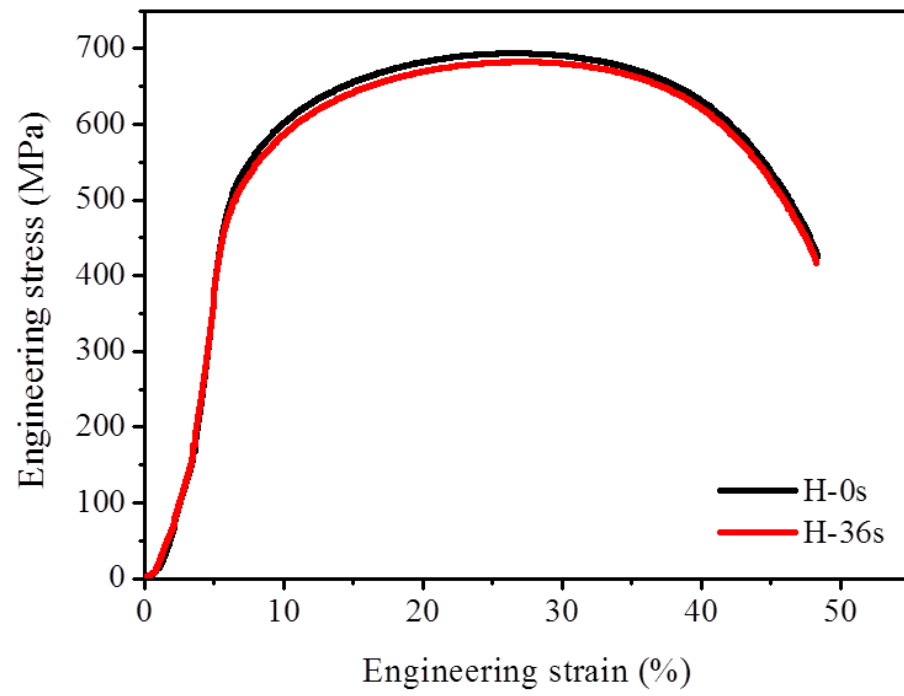
Figure 4.14 Engineering stress-strain curves of tensile tests.

4.4 Conclusions

In the present study, dissimilar SUS316L and IN718 alloys were successfully joined by EAPJ at a temperature significantly lower than the melting points of the BMs. The microstructural analysis and mechanical tests consistently showed that a sound solid state joint was fabricated for the dissimilar material combination without complicated rotating and braking equipments (in comparison with friction welding) with a short process time (in comparison with pressure joining). The results of tensile tests clearly showed that the strength of the joint interface surpasses the strength of the SUS316L alloy in the joint, even without additional holding time at elevated temperature, as demonstrated by a ductile fracture occurring in the middle of the SUS316L side. The effectiveness of the EAPJ for dissimilar joining shown in the present study suggests that the concept of EAPJ is promising for joining various structural components. However, for the material combination selected in the present study, it should be noted that further evaluation of fatigue properties is still necessary to confirm the industrial applicability of EAPJ to the combined SUS316L and IN718 alloys.

References

Choi J, Mazumder J (2002) Numerical and experimental analysis for solidification and residual stress in the GMAW process for AISI 304 stainless steel, Journal of Materials Science. 37:2143–2158.

Cortes R, Barragan ER, Lopez VH, Ambriz RR, Jaramillo D (2018) Mechanical properties of Inconel 718 welds performed by gas tungsten arc welding, International journal of Advanced Manufacturing Technology. 94:3949-3961.

Damodaram R, Ganesh Sundara Raman S, Prasad Rao K (2013) Microsturcture and mechanical properties of friction welded alloy 718, Materials Science & Engineering A. 560:781-786.

Ferretti S, Valenzano G, Cugno W (2006) International space station external active thermal control system lines manufacturing, the 57th International Astronautical Congress Proceeding, October 2-6. Valencia, Spain.

Harada Y, Sada Y, Kumai S (2016) Joining steel studs and steel plates by solid-state stud welding and estimation of temperature near the joint interface, Journal of Manufacturing Processes. 23:75-82.

Henderson MB, Arrellb D, Larsson R, Heobel M, Marchant G (2004) Nickel-Based superalloy welding practices for industrial gas turbine applications, Science and Technology of Weld & Joining. 9(1) :13-21.

Hinojos A, Mireles J, Reichardt A, Frigola P, Hosemann P, Murr LE, Wicker RB (2016) Joining of Inconel 718 and 316 stainless steel using electron beam melting additive manufacturing technology, Materials and Design. 94:17-27.

Hong ST, Chun DM, Park HS, Han HN, ParkJW, Li YF, Nguyen DS (2018) Electrically assisted pressure joining apparatus and method, KR Patent No. 10-1921053.

Hong ST, Li YF, Park JW, Han HN (2018) Effectiveness of electrically assisted solid-state pressure joining using an additive manufactured porous interlayer, CIRP Annals-Manufacturing Technology. 67(1):297-300.

Iturbe A, Hormaetxe E, Garay A, Arrazola PJ (2016) Surface integrity analysis when machining inconel 718 with conventional and cryogenic cooling, Procedia CIRP. 45: 67-70.

Kim MJ, Lee MG, Hariharan K, Hong ST, Choi IS, Kim D, Oh KH, Han HN (2017) Electric current-assisted deformation behavior of Al-Mg-Si alloy under uni-axial tension, International Journal of Plasticity. 94:148–170.

Kim MJ, Lee KH, Oh KH, Choi IS, Yu HH, Hong ST, Han HN (2014) Electric current-induced annealing during uniaxial tension of aluminum alloy, Scripta Materialia. 75:58–61.

Kumara SS, Muruganb N, Ramachandranc KK (2018) Microstructure and mechanical properties of friction stir welded AISI 316L austenitic stainless steel joints, Journal of Materials Processing Technology. Tech. 254:79-90.

Li YF, Das H, Hong ST, Park JW, Han HN (2018) Electrially assisted pressure joining of titanium alloy, Journal of Manufacturing Processes. 35:681-686.

Lin HL, Wu TM, Cheng CM (2014) Effects of flux pre-coating and process parameter on welding performance of inconel 718 alloy TIG welds, Journal of Materials Engineering & Performance. 23:125-132.

Liu FC, Nelson TW (2018) Grain structure evolution, grain boundary sliding and material flow resistance in friction welding of Alloy 718, Materials Science & Engineering A. 710:280-288.

Locci IE, Bowman CL, Gabbs TP (2009) Development of high temperature dissimilar joint technology for fission surface power systems, Proceedings of the 4th International Brazing and Soldering Conference, April 26-29. Hilton in the Walt Disney World Resort, Orlando, Florida. USA.

Martinsen K, Hu SJ, Carlson BE (2015) Joining of dissimilar materials, CIRP Annals-Manufacturing Technology. 64(2):679–699.

Mori K, Bay N, Fratini L, Micari F, Tekkaya AE (2013) Joining by plastic deformation, CIRP Annals - Manufacturing Technology. 62(2):673–694.

Naffakh H, Shamanian M, Ashrafizadeh F (2009) Dissimilar welding of AISI 310 austenitic stainless steel to nickel-based alloy Inconel 657, Journal of Materials Processing Technology. 209:3628-3639.

Ng MK, Li L, Fan Z, Gao RX, Smith III EF, Ehmann KF, Cao J (2015) Joining sheet metals by electrically-assisted roll bonding, CIRP Annals – Manufacturing Technology. 64(1):273-276.

Park JW, Jeong HJ, Jin SW, Kim MJ, Lee K, Kim JJ, Hong ST, Han HN (2017) Effect of electric current on recrystallization kinetics in interstitial free steel and AZ31 magnesium alloy, Materials Characterization. 133:70–76.

Peng L, Xu Z, Lai X (2014) An investigation of electrical-assisted solid-state welding/bonding process for thin metallic sheets: experiments and modeling,

Proceedings of the Institution of Mechanical Engineers, Part B: Journal of Engineering Manufacture. 228(4):582-594.

Ramkumar KD, Patel SD, Praveen SS, Choudhury DJ, Prabaharan P, Arivazhagan N, Xavior MA (2014) Influence of filler metals and welding techniques on the structure-property relationships of Inconel 718 and AISI 316L dissimilar weldments, Materials and Design. 62:175-188.

Ramkumar T, Selvakumar M, Narayanasamy P, Begam AA, Mathavan P (2017) Studies on the structural property, mechanical relationships and corrosion behavior of Inconel 718 and SS 316L dissimilar joints by TIG welding without using activated flux, Journal of Manufacturing Processes. 30:290-298.

Roh JH, Seo JJ, Hong ST, Kim MJ, Han HN, Roth JT (2014) The mechanical behavior of 5052-H32 aluminum alloys under a pulsed electric current, International Journal of Plasticity. 58:84-99.

Smith M, Bichler L, Gholipour J, Wanjara P (2016) Mechanical properties and microstructural evolution of in-service Inconel 718 superalloy repaired by linear friction welding, International Journal of Advanced Manufacturing Technology. 90(5-8):1931-1946.

Tharappel JT, Babu J (2018) Welding processes for Inconel 718- A brief review. IOP Conference Series: Materials Science and Engineering. 330: 012082.

Xu Z, Peng L, Yi P, Lai X (2013) Study on a novel electrical-assisted pressure welding process of thin metallic foils, Applied Mechanics and Materials. 271– 272:147–151.

CHAPTER V

CONCLUSIONS

EAPJ is one of the Electrically-assisted manufacturing (EAM) technologies, which utilizes electricity to any manufacturing process. In EAPJ, an electric current is directly applied to the specimen during plastic compression. In comparison to conventional pressure joining, using resistance heating as a heat source provides several technical advantages. First, the workpieces can be heated rapidly and locally. As a result, the process time can be reduced and unnecessary thermal effects on the workpiece can be minimized. Also, the joining apparatus can be significantly simpler and cost-effective, as the need for a heating furnace can be eliminated. The concept of EAPJ also provides technical advantages over friction welding in the joining of bulk workpieces. By using resistance heating as a heat source, the need for complex rotation and brake systems can be eliminated. Also, since the heating of the interface can be continued during the final axial compression, process optimization is relatively easier. EAPJ is a promising technology which can bond similar or dissimilar various sheet and bulk metals with very short process time (just few seconds). However, nowadays studies on EAPJ of metal alloys are still limited and are mostly conducted on very thin foils.

The dissertation demonstrates the joining feasibility of Ti/Ti alloy sheets, SUS316L/SUS316L cylindrical bulk steel and SUS316L/IN718 cylindrical bulk steel by EAPJ. Also, in order to improve the process effectiveness, the EAPJ of SUS316L/SUS316L cylindrical bulk components using an additive manufactured metal porous interlayer is

demonstrated. The major achievements/findings of this dissertation can be summarized as follow:

- Grade 1 Ti alloy sheets with thickness of 1 mm were successfully joined by EAPJ at temperatures significantly lower than the melting temperature of the alloy. The results of OM and EBSD analysis confirmed that a sound solid-state joint was successfully fabricated by EAPJ due to the diffusion of atoms and recrystallization under the combined action of electric current and compression. The joining load (or thickness reduction) needed for EAPJ can be reduced rapidly by increasing current intensity. The lap shear tensile tests showed that thickness reduction and current intensity have significant effects on the mechanical behavior of the joint. An optimal thickness reduction, corresponding to the maximum fracture load, exists for each value of current intensity, and decreases as current intensity increases. A higher fracture load can be obtained by adjusting the combination of the current intensity and the thickness reduction parameters. The results of the present study provide a design guide for the optimization of lap joining by EAPJ.

- Effectiveness of using an additive manufactured metal porous interlayer during EAPJ of bulk specimens was demonstrated. By using the porous interlayer with a lower compressive strength and higher electric resistivity, defect-free joints were successfully fabricated with a lower joining pressure. As confirmed by the microstructural analysis, the porosity in the interlayer was eliminated by the compressive deformation and recrystallization during joining. In fact, the occurrence of grain growth in the joints with the interlayer suggests that the

process effectiveness can be further enhanced by adjusting the temperature profiles during EAPJ. The results of the microhardness measurement and cantilever bend test showed that the mechanical properties of the joints with the interlayer are comparable to those of the joint without the interlayer. The result of the present study can be expanded to solid-state joining of dissimilar (or even difficult to weld) bulk components by properly adjusting the structure and chemical composition of the porous interlayer.

- Dissimilar SUS316L and IN718 alloys were successfully joined by EAPJ at a temperature significantly lower than the melting points of the BMs. The microstructural analysis and mechanical tests consistently showed that a sound solid state joint was fabricated for the dissimilar material combination without complicated rotating and braking equipments (in comparison with friction welding) with a short process time (in comparison with pressure joining). The results of tensile tests clearly showed that the strength of the joint interface surpasses the strength of the SUS316L alloy in the joint, even without additional holding time at elevated temperature, as demonstrated by a ductile fracture occurring in the middle of the SUS316L side. The effectiveness of the EAPJ for dissimilar joining shown in the present study suggests that the concept of EAPJ is promising for joining various structural components. However, for the material combination selected in the present study, it should be noted that further evaluation of fatigue properties is still necessary to confirm the industrial applicability of EAPJ to the combined SUS316L and IN718 alloys.